

Segmentation of arbitrary features in very high resolution remote sensing imagery

Henry Cording^{1,2,*}, Yves Plancherel¹, and Pablo Brito-Parada¹

¹Department of Earth Science and Engineering, Imperial College London, London SW7 2AZ, United Kingdom

²Vattenfall Europe Information Services GmbH, Berlin 10829, Germany

*Address correspondence to: henry.cording@pm.me

Abstract

Very high resolution (VHR) mapping through remote sensing (RS) imagery presents a new opportunity to inform decision-making and sustainable practices in countless domains. Efficient processing of big VHR data requires automated tools applicable to numerous geographic regions and features. Contemporary RS studies address this challenge by employing deep learning (DL) models for specific datasets or features, which limits their applicability across contexts.

The present research aims to overcome this limitation by introducing EcoMapper, a scalable solution to segment arbitrary features in VHR RS imagery. EcoMapper fully automates processing of geospatial data, DL model training, and inference. Models trained with EcoMapper successfully segmented two distinct features in a real-world UAV dataset, achieving scores competitive with prior studies which employed context-specific models.

To evaluate EcoMapper, many additional models were trained on permutations of principal field survey characteristics (FSCs). A relationship was discovered allowing derivation of optimal ground sampling distance from feature size, termed Cording Index (CI). A comprehensive methodology for field surveys was developed to ensure DL methods can be applied effectively to collected data.

The EcoMapper code accompanying this work is available at [this https URL](#).

1 Introduction

Over the last four decades, the spatial resolution of both satellite and unmanned aerial vehicle (UAV) imagery has improved rapidly [1], reaching 30–50 cm/pixel for privately owned satellites [2, 3], and less than 1 cm/pixel for UAVs [4, 5, 6]. These developments enable species-specific recognition [7, 8] and feature identification at up to centimetre scale [9, 10, 11]. Concurrently, increases in spatial and temporal resolution call for new data processing capabilities [12]. As a result, machine learning and in particular deep learning (DL) methods have seen several adaptations for automated analysis of remote sensing (RS) imagery in recent years [13, 14, 15].

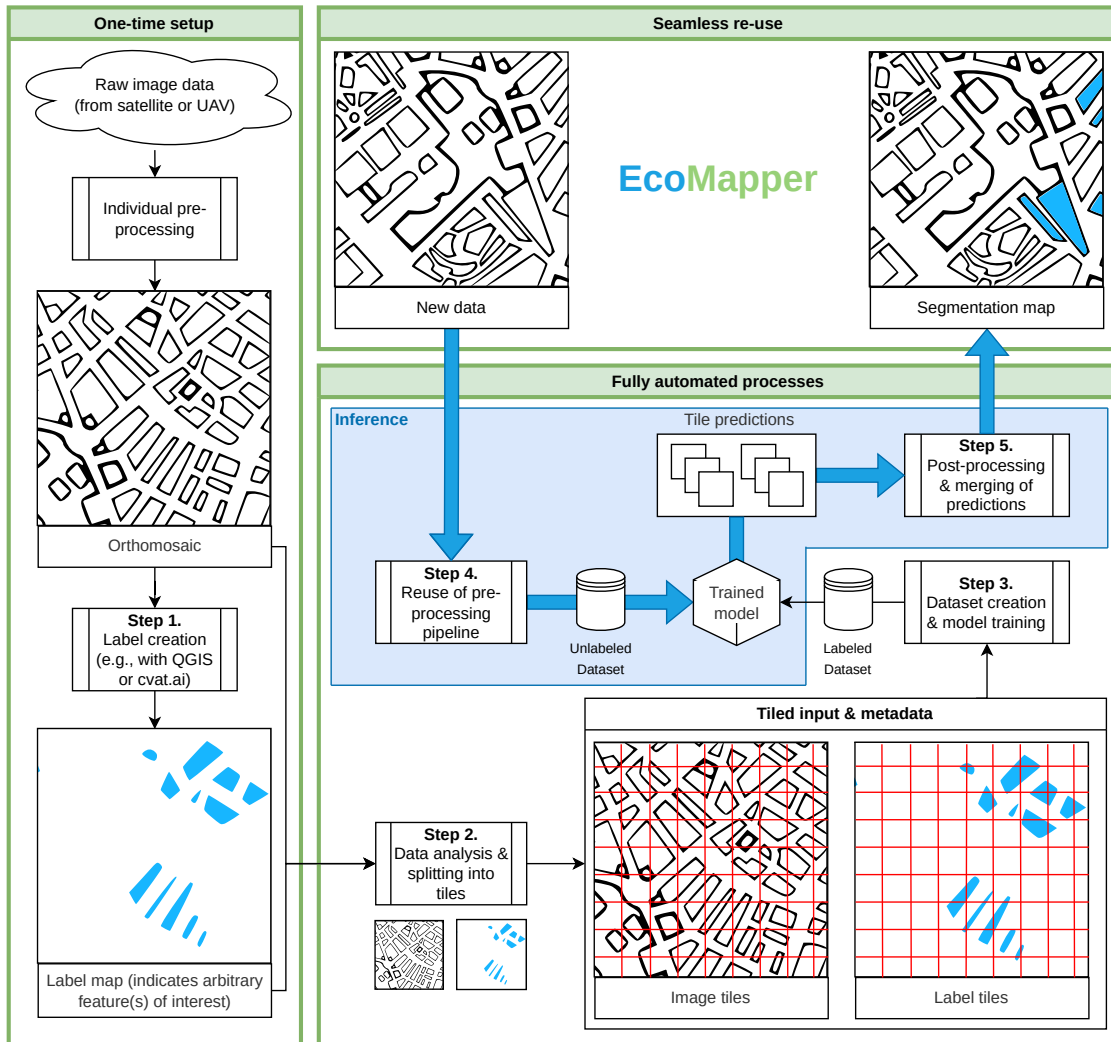


Figure 1: A high level overview of EcoMapper’s architecture. Data pre- and post-processing, as well as model training, evaluation, and inference are fully automated.

With the availability of very high resolution (VHR) RS imagery and increasingly powerful DL models, a novel opportunity emerges to map a multitude of features, such as insects and fauna, at centimeter scale across entire landscapes. This would facilitate biodiversity monitoring at very high temporal resolution, to oversee endangered species and support their rehabilitation.

In the context of climate change, VHR mapping could provide detailed insights into changes in land cover, vegetation health, and water resources, which are critical for understanding the impacts of climate change [16, 17, 18, 19]. VHR mapping could also enable resource valuation and management on an unprecedented scale, to aid in establishing sustainable practices such as precision agriculture.

In sum, the development of robust systems for VHR mapping could prove invaluable for informing decision-making and sustainable development globally.

1.1 Problem Description

A major issue in contemporary RS research preventing large scale VHR mapping is the strong fluctuation in how DL models are designed and used. Many studies focus on building custom models to perform well on particular datasets or features, visible clearly in surveys on the use of DL in RS [13, 14, 15]. Literature review additionally revealed a conspicuous lack of standardized DL workflows [7, 8, 9, 20, 21].

This makes results hard to reproduce, especially since code is rarely open sourced [22, 23], which adds to the already high barrier of entry to leverage DL that arises from model complexity and computational cost [13]. Most importantly, with researchers tailoring their own models to specific datasets, transferability of implementations is hindered. This is despite VHR RS imagery being extremely diverse, containing countless features whose size and spectral properties can vary significantly. It therefore cannot be feasible to design entire models and workflows anew for each feature to be studied.

1.2 A case for EcoMapper

To address the shortcomings of context-specific solutions, this research introduces EcoMapper¹, a DL-based application for semantic segmentation of arbitrary features in VHR RS imagery. Designed to provide a reusable and configurable approach to feature segmentation, the aim of EcoMapper is to reduce duplicate RS research efforts and aid the reproducibility of results, while also democratizing access to DL technology. An overview is provided in Fig. 1.

Semantic segmentation divides an image into segments, where each segment identifies an object class (e.g., car, pedestrian, building). Although semantic segmentation is not the only computer vision task in RS, along with Land Use/Land Cover (LULC) classification it constitutes a significant portion of contemporary RS research [14]. Notably, LULC classification can be addressed with semantic segmentation models [24], thus EcoMapper presents a generalizable solution to a large problem space in RS.

Solutions related to EcoMapper exist but are either not applicable to RS data, or fail to eliminate the need for specific models to be designed on a per use case basis. They are discussed below.

1.2.1 Raster Vision

Raster Vision [25] is a library and framework for applying DL to RS imagery. It supports several geospatial data formats and implements processing routines to make RS data compatible with DL model training. Raster Vision can be used as a library for training existing PyTorch models with RS data, but also provides a framework to train prebuilt models on RS imagery. There are several reasons why Raster Vision is not suitable for repeated application across data- and feature-sets, which is the main goal of EcoMapper.

Model selection. Raster Vision provides only a limited selection of prebuilt models via the PyTorch Hub [26], which does not feature recent state-of-the-art models. Recently published models thus need

¹<https://github.com/hcording/ecomapper>

to be implemented or sourced manually. As motivated in section 1, there is need for a solution in which the choice of model is abstracted away. Section 2.3 will show that model training in EcoMapper was integrated with the MMSegmentation library [27], making it trivial to update or swap models, unlike in PyTorch (or similar libraries).

Ease of use. Raster Vision requires programming experience even for the simplest use cases. Python script files need to be written to describe a particular task to the framework. In contrast, EcoMapper was developed under a ready-to-use paradigm – while it can easily be extended programmatically, e.g., to use a different model for segmentation, the published version can be run from the commandline without writing any code; and it is still applicable to any dataset and feature(s) of interest.

Data labeling support. Raster Vision does not integrate with data labeling tools, which are an integral part of segmentation workflows. Section 2.2 will detail measures taken to integrate EcoMapper with various labeling tools and formats, providing a solution that covers the entire segmentation workflow, and is accessible to users without prior labeling experience.

1.2.2 Segment Anything

The Segment Anything Model (SAM) [28] is a recent zero-shot segmentation model developed by Meta (Facebook). As the name suggests, the model is intended for segmenting arbitrary scenes without requiring additional tuning.

SAM was trained on the very diverse Segment Anything dataset [28], with no particular feature focus, to cover as many use cases as possible. This makes it a robust solution for segmenting commonly occurring features. The model can either be used interactively by clicking on image regions to include or exclude, or it can segment a scene autonomously.

EcoMapper produces models which specialize on particular features of interest. These models outperform SAM when studying features that are underrepresented in day-to-day imagery. As shown in appendix A, using SAM the segmentation of a unique feature requires several guiding inputs from the user, and fails entirely in the autonomous mode. The model trained by EcoMapper manages to segment the feature precisely and without aid.

Lastly, SAM does not provide any means for pre- or post-processing of geospatial data, which is a key component of EcoMapper, and introduces non-trivial challenges for training DL models.

1.3 Challenges in applying EcoMapper across varying real-world contexts

A solution like EcoMapper is urgently required to cope with processing demands of large scale VHR data. However, EcoMapper is not a holistic solution to arbitrary feature segmentation, due to interdependency with field survey characteristics (FSCs). FSCs dictate the amount and quality of data available for DL model training. Feature size, image resolution, and survey extent affect DL model performance and the cost, duration, and feasibility of field surveys. A comprehensive surveying methodology must be developed to respect surveying resources and ensure effective application of DL to collected data.

Impacts of FSCs on DL performance must be understood to build a DL-informed surveying method. Prior studies selectively reviewed resolution, feature size, or dataset size as influencing factors on model performance, but a combination of factors was not considered in depth.

In [9] and [29], the impact of ground sampling distance (GSD) on DL performance was described. GSD measures the distance on Earth’s surface covered by the width (or height) of a single pixel. GSD has a large impact on model performance [9, 29, 21], but the impact is dependent on feature size [30] as larger features are more visible in low resolution imagery. In [30] the effect of feature size on performance was demonstrated, but without discussing a general relationship between feature size and GSD. Effects of survey extent and dataset size on DL performance in RS studies are discussed even more sparingly [31, 32].

1.4 Research gaps & objectives of this study

To summarize, the following research gaps emerge:

1. DL models are applied to specific use cases. Introduction of VHR imagery and abundance of visible features call for a more widely applicable solution to feature extraction.
2. A generalizable DL solution requires a surveying methodology that links FSCs to DL, ensuring applicability of DL to collected data.

To address the prior shortcomings, the following objectives were posed for this study:

1. To design EcoMapper for automatic segmentation of arbitrary features in VHR RS imagery, without requiring dataset-specific model tuning.
2. To simulate principal FSCs, such as resolution, feature size, and survey extent, and evaluate their effects on model performance.
3. To design a generalizable field survey workflow to accommodate for FSCs and the application of DL.

2 Methodology

A real-world UAV dataset was first obtained (section 2.1) and two distinct features were labeled (section 2.2). EcoMapper was then developed (section 2.3) without specific considerations to the dataset at hand. Models were repeatedly trained with EcoMapper to simulate several permutations of FSCs (section 2.4). Multiple degradation methods were considered to synthetically reduce GSD. Lastly, experiments were set up and run on the HPC platform of Imperial College London (section 2.5).

2.1 Dataset overview

For this study, an RGB orthomosaic (perspective-normalized stitching of many, partially overlapping images) was used. The image mapped approximately 3 km² of the Sto. Niño legacy mining site in

Tublay, Philippines. An excerpt is depicted in appendix B. A DJI Mavic 3 MS drone equipped with a 20MP sensor was flown at 50 metre altitude to capture this data, yielding a GSD of 0.022 m/px. Images were taken in March 2023.

2.2 Labeling methods and integration with EcoMapper

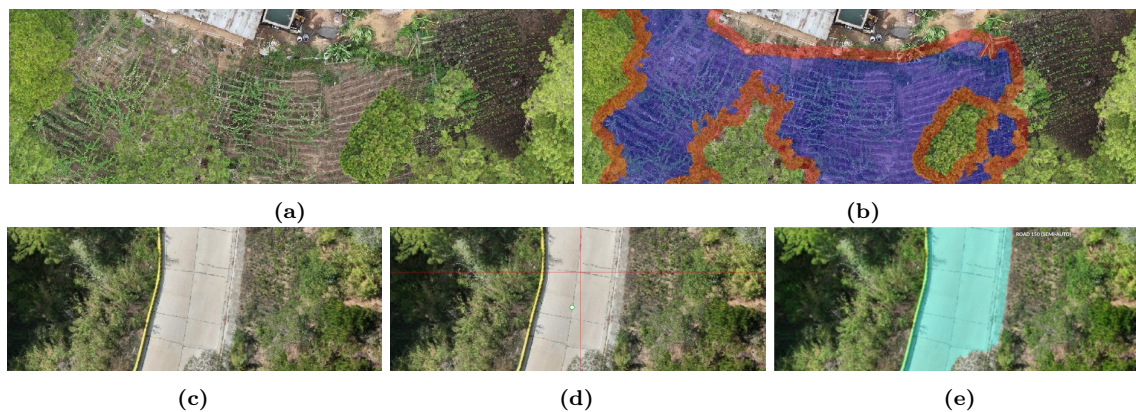


Figure 2: Overview of the labeling process. Top row: QGIS labeling. (a) Partial view of a Chayote plantation in the Sto. Niño region; (b) an overlay of the manually drawn label map for Chayote, labels were palettized for visualization. Blue indicates “Chayote”, red indicates “Border” (uncertainty). Bottom row: CVAT labeling. (c) Input image; (d) points are placed indicating the feature to label; (e) the label (cyan) is generated automatically by CVAT.

Data were labeled manually using QGIS [33], and CVAT [34] which employs DL models to accelerate labeling. Fig. 2 illustrates the labeling workflow. In support of reproducible research, instructional videos were recorded explaining the labeling procedure in QGIS. EcoMapper is compatible with CVAT labels, and a video was recorded explaining the use of CVAT and how to import results into EcoMapper. Details and video URLs are documented in appendix C.

Chayote plantations (appendix D) were chosen as initial feature to label and segment. A “border” class was introduced to indicate uncertainty w.r.t. where plantations end and the background starts. Roads were labeled (Fig. 2c–2e) to investigate whether EcoMapper could segment a feature with vastly different size and spectral properties. Roads did not have a border class as they were easily distinguished from the background.

2.3 Development of the EcoMapper pipeline

EcoMapper was developed as OS-independent application with a commandline interface (CLI) using Python. The project’s code repository features thorough installation and usage instructions. Sphinx [35] was used to organize code documentation into HTML format. The `pip-tools` library [36] was utilized to generate an exhaustive file of pinned requirements, aiding build reproducibility. Integration of the GDAL library [37] to work with geospatial data was achieved with Anaconda [38], to avoid complications with OS-specific packages otherwise required by GDAL. All software used during EcoMapper’s development is free and open source.

2.3.1 Architecture

Three components make up the pipeline illustrated in Fig. 1: Data preprocessing, model training/evaluation, and postprocessing of model predictions into a segmentation map. EcoMapper is built up from “Tasks” to abstract these steps. For example, model training is implemented through the `TrainTask`. In appendix E the network of Tasks and their interdependencies are depicted. The CLI can either run the full pipeline (all tasks in sequence) or run any Tasks in isolation, e.g., to prepare a dataset for future training on a different machine.

Several notable features were built into EcoMapper, including multiprocessing, support for a wide range of hardware, and the ability to work with a multitude of geospatial image and label formats. A complete description can be found in appendix F.

2.3.2 Preprocessing – Data fragmentation and dataset creation

Inputs to DL models are small, typically 512x512 pixels or less, but geospatial data are far larger. Splitting RS imagery is challenging because orthomosaics typically do not fit into memory. Prediction artifacts at tile boundaries can also arise since adjacent tiles are input separately to the model.

Input images to EcoMapper are memory mapped (read incrementally from disk, instead of at once). A sliding window is used to introduce overlap between tiles. Blending tiles significantly increases prediction coherence, and provides $(1/s)^2$ times more data for model training, where $0 < s < 1$ is the stride ($s = 0.5$ was chosen here). The resulting image and label tiles are stored in compressed JPG format at 90% quality and PNG format (lossless compression), respectively. Georeference information in the input is saved and later restored, so the predicted segmentation map can again be imported into GIS software and will be positioned correctly.

2.3.3 MMSegmentation integration

DL research advances rapidly. For EcoMapper to be a future-proof solution, manual implementation of semantic segmentation models from scratch was deemed unsuitable.

Instead, MMSegmentation [27] was integrated to facilitate model training. MMSegmentation is an actively maintained library for semantic segmentation, developed by OpenMMLab [39]. The library has been used in many prior studies (e.g., [40, 41, 42]) and contains numerous state-of-the-art DL models for semantic segmentation. New models are added regularly as research progresses. MMSegmentation centers around simple configuration files with a high degree of abstraction, which result in the creation of PyTorch models in the backend. Updating or replacing models is therefore simplified compared to direct use of PyTorch or other DL libraries.

Training strategies. EcoMapper extends the MMSegmentation training procedure to mitigate class imbalance between features and the background. The pipeline calculates the class distribution over the training dataset and assigns a weight to each tile, as shown in appendix G.1. These weights are used during training to oversample minority class(es) for each batch of training data.

Samples are then subjected to randomized image augmentations, using the Albumentations [43] library. Augmentations such as downscaling and color shift help reduce overfitting on the training

set [44, 45, 46]. By increasing the variety of tiles when oversampling minority classes, the likelihood of having identical tiles in a batch is reduced.

Splitting data for training and evaluation. RS data are spatially auto-correlated [47], meaning the distance between pixels influences their similarity. Thus, the assumption of independent and identically distributed (IID) random variables does not hold, and regular DL approaches to shuffle and split data must be avoided.

EcoMapper offers two splitting methods. The first method divides the dataset into train, validation, and test sets along the horizontal line. After the split, only the train set is shuffled. Method 1 addresses the problem of spatial leakage, but can lead to suboptimal proportions of non-background samples in each set. In the worst case, the training set only contains background samples, giving the model nothing to train on.

Method 2 allows users to manually split data with QGIS. The resulting sets with balanced class distribution can be passed to EcoMapper for automatic model training and evaluation using three datasets.

2.3.4 Postprocessing – Merging model predictions

As image tiles partially overlap, so do the model’s predictions. Merging of predictions is non-trivial and can heavily impact segmentation map quality. Appendices G.2 and G.3 outline considered strategies, including visual comparison of merge results.

The first approach (logit-merge) merges overlapping tiles using the model’s confidences (logits). Method two (crop-merge) crops overlapping tiles, such that only the center of tiles is used (except at image boundaries). Crop-merging generates higher quality results and executes faster.

2.4 Simulating survey characteristics

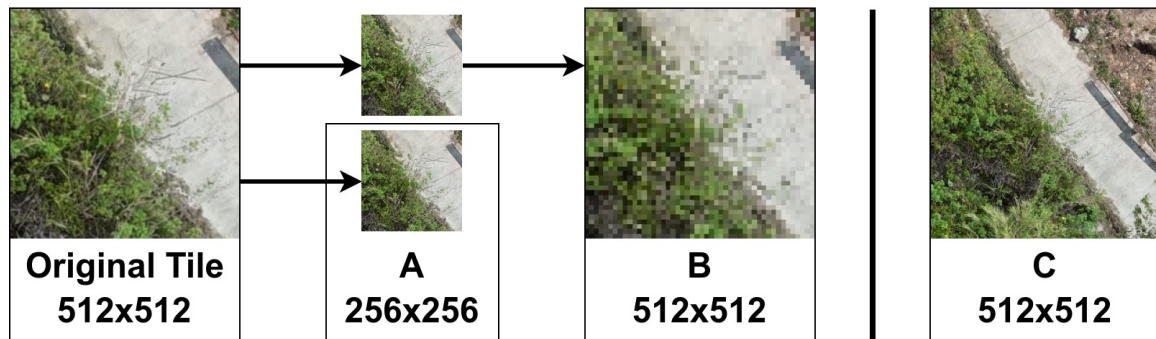


Figure 3: Methods of resolution degradation. The original image (top left) can be downsized (A), downsized and upscaled to the original tile dimensions (B), or the original orthomosaic can be downsized and split into tiles anew, yielding fewer tiles that cover more spatial distance and appear “zoomed out” (C).

As argued in section 1, a meaningful evaluation of EcoMapper had to consider principal survey characteristics: feature size, GSD, and survey extent. To study the effect of feature size, models were trained on Chayote plantations and roads which have vastly different size (and spectral properties).

To study the impacts of GSD, per feature models were trained on 12 versions of the dataset with decreasing GSD. The 9 lowest GSDs were chosen from satellites capturing VHR imagery, to gauge the viability of satellite data for VHR studies. Appendix H lists all considered GSDs; due to computational constraints, the highest considered resolution was 0.08 m/px.

Different synthetic degradation methods were applied to reduce GSD, as illustrated in Fig. 3. Appendix I describes each method in detail. Note that method B only degrades images, while leaving labels at native quality. Investigating multiple degradation methods is necessary to identify a general trend in performance degradation, making the evaluation more robust to particularities of individual methods.

Lastly, models were trained on the original data with a decreasing number of images in the training set, to simulate the effect of survey extent on model performance. A total of 99 models were trained for this study.

2.5 Model training

The Mask2Former [48] model was chosen for semantic segmentation. It is a vision transformer (ViT) based deep neural network which achieved state-of-the-art performance on the competitive Cityscapes [49] and ADE20K [50] segmentation benchmarks in 2021/22. A more detailed overview is given in appendix J. The choice of model in EcoMapper is largely interchangeable due to use of MMSegmentation, but Mask2Former was chosen primarily because it performed best in the aforementioned benchmarks, and using a strong baseline for transfer training on specific features was crucial to enable generalizability of EcoMapper.

2.5.1 Experimental setup

The high performance computing (HPC) platform of Imperial College London was utilized for model training. Models were trained using one NVIDIA RTX6000 GPU (Turing, driver 535.54.03) with 24 GB VRAM, 32 GB of system RAM, and 4 CPU cores.

All runs utilized the same CUDA (11.7), PyTorch (2.0.1+cu117) and TorchVision (0.15.2+cu117) versions, which are fixed by EcoMappers’s pip environment. The same seed for all libraries was used throughout the research project. These precautions alone do not guarantee identical results on other hardware, but they make up for the largest fluctuations in model performance. Fixing the batch size and seed guarantees that the model receives samples in the same order on each training run, regardless of the hardware used.

To mitigate spatial leakage and achieve a stable class distribution, the orthomosaic and label maps were split manually into approximately 70% train, 10% validation, and 20% test data, as illustrated in Fig. 4. Models were configured with a Swin-S backbone [51] pretrained on the Cityscapes dataset [49]; given the substantial differences in scenery and viewing angle in the Sto. Niño dataset, the backbone was not frozen to give the model more flexibility during transfer training.

For each resolution and degradation method, models were transfer-trained over 90 epochs with a batch size of 12 and learning rate of $1e-4$, using the AdamW optimizer [52]. With the default Mask2Former configuration in MMSegmentation, the optimizer used a weight decay of 0.05, $\epsilon = 1e-8$,

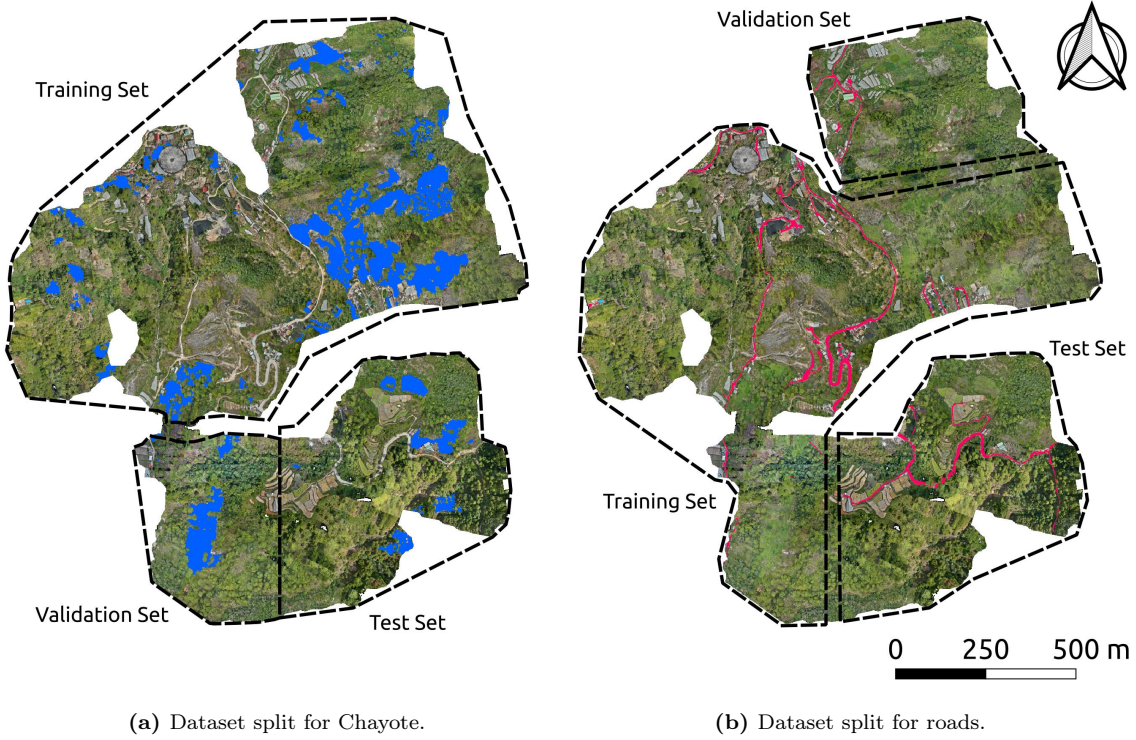


Figure 4: Training, validation, and test sets after manually labeling and splitting the Sto. Niño dataset. Ground truth labels are indicated, showing a favorable distribution of classes in all three sets for both features. Spacing was introduced between the train and evaluation sets to reduce spatial leakage.

and $\beta = (0.9, 0.999)$. Except for two models, the validation loss during training always plateaued before reaching 90 epochs. Model weights with the lowest validation loss were chosen for testing. No hyperparameter tuning was conducted; as detailed in section 1, EcoMapper aims to apply to arbitrary features and datasets, without requiring adjustments on a per-use-case basis.

The intersection over union (IoU) and Dice coefficient (F1 score) were used for model evaluation, which are among the most prominent benchmarking metrics in the literature. IoU measures how well predictions overlap with ground truth labels. The Dice coefficient is the harmonic mean of precision and recall: Precision describes the fraction of positive predictions that are correct, recall gives the proportion of positive samples that the model correctly predicted as positive. The formulas are given below.

$$\text{IoU} = \frac{TP}{TP + FN + FP} = \frac{|\hat{Y} \cap Y|}{|\hat{Y} \cup Y|} \quad (1)$$

$$\text{Dice coefficient} = \frac{2TP}{2TP + FN + FP} = \frac{2|\hat{Y} \cap Y|}{|\hat{Y} \cap Y| + |\hat{Y} \cup Y|} = \frac{2|\hat{Y} \cap Y|}{|\hat{Y}| + |Y|} \quad (2)$$

Where TP , FP and FN are true positives, false positives, and false negatives, respectively. \hat{Y} and Y are predictions and ground truth, with \cap and \cup denoting intersection and union.

3 Evaluation

3.1 Profiling of EcoMapper performance

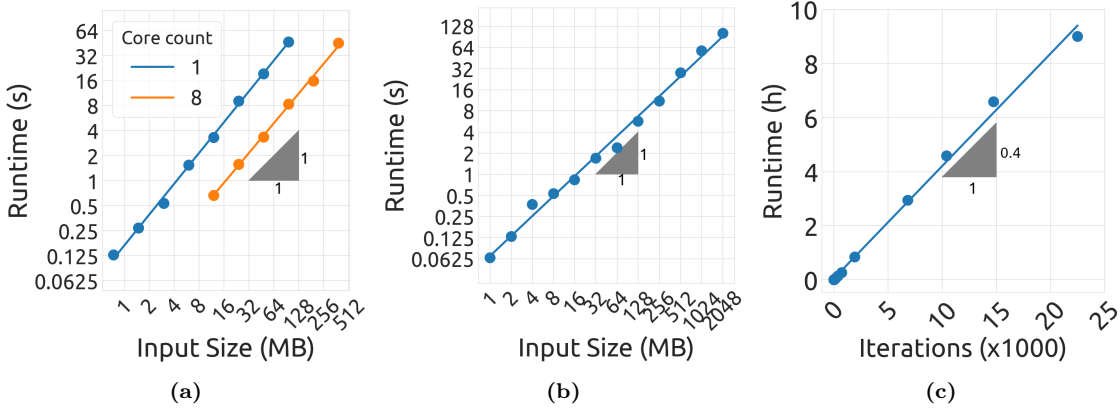


Figure 5: EcoMapper performance in different tasks. (a) Image splitting using a stride of 0.5; (b) prediction merging, input size indicates total size of all tiles; (c) GPU training with PyTorch via MMSegmentation.

Code profiling was conducted to measure the efficiency of data processing and model training code of EcoMapper, see Fig. 5. Algorithms for image splitting and merging predictions naturally had time complexities of $\mathcal{O}(nm)$, as they iterate over the $n \times m$ input image once. Model training implemented in PyTorch also scaled linearly with input size, and benefited heavily from GPU acceleration.

However, significant differences in runtime still arose and were managed. EcoMapper’s algorithm to split an input image operated at a stride of 0.5, thus the actual amount of work per image increased by factor 4. The operation was accelerated by distributing the image rows over all cores. Merging tiles, while also $\mathcal{O}(n)$, was accelerated significantly using the crop-merge algorithm, mainly due to use of vectorized NumPy operations implemented in C to copy tile contents into the merged segmentation map.

3.2 Semantic segmentation of Chayote and roads using EcoMapper

Table 1: Per-feature test scores of Mask2Former instances trained with EcoMapper on the Sto. Niño dataset (0.08 m/px). Main scores were obtained by summing the scores of individual tiles before computing the overall ratio. Scores in parentheses are calculated after merging predictions into a single image using the crop-merge strategy.

Feature	mIoU	mDice	Background IoU	Feature IoU	Border IoU
Chayote	0.668 (0.682)	0.748 (0.760)	0.986 (0.992)	0.792 (0.814)	0.225 (0.240)
Roads	0.798 (0.831)	0.875 (0.900)	0.995 (0.995)	0.610 (0.667)	n/a

The models trained with EcoMapper achieved mean IoUs (mIoU) of 0.668 and 0.798 for Chayote and roads, respectively (Tab. 1). Chayote scores were skewed by the border class, which the model did

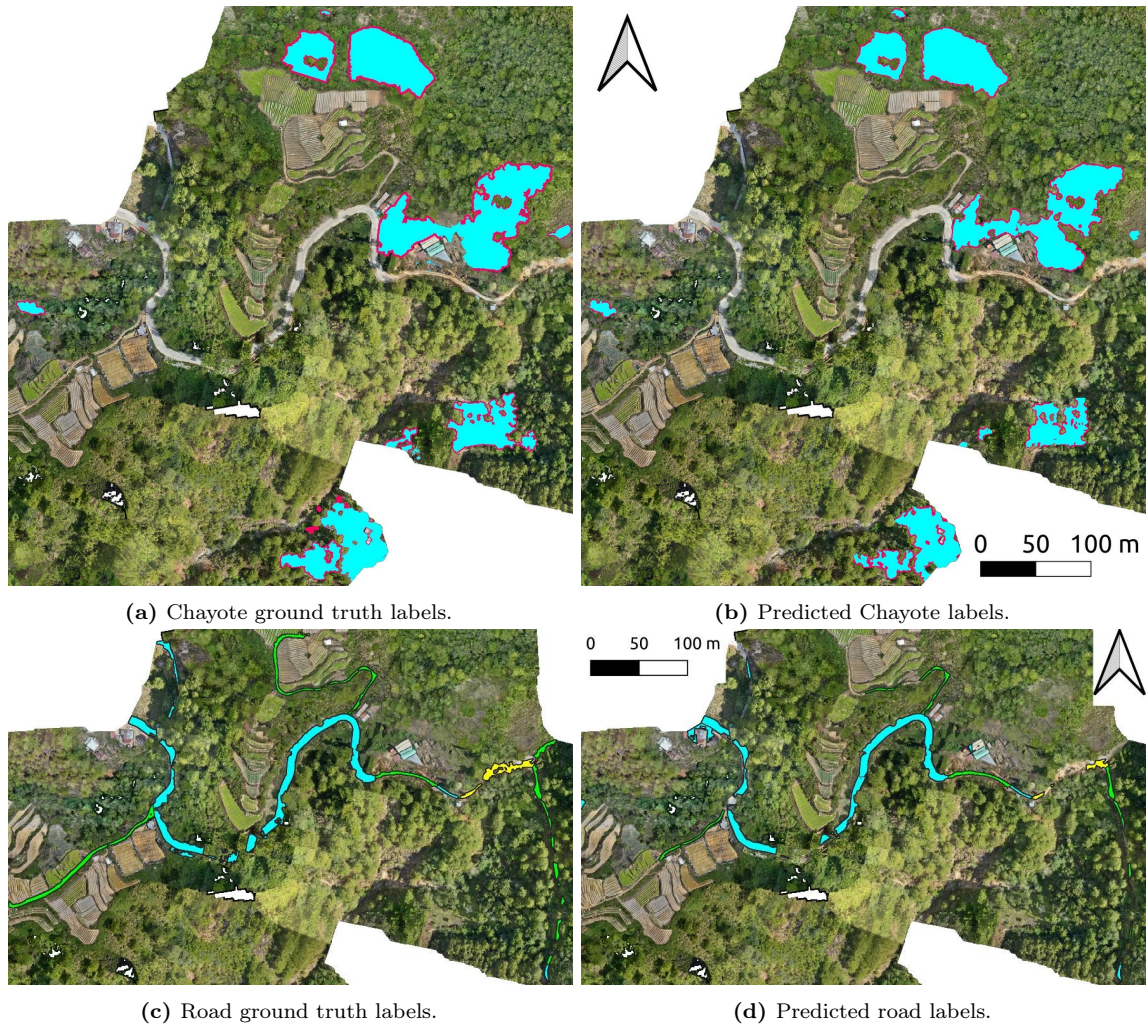


Figure 6: Comparison of ground truth with model predictions in the test set. For (a) and (b), cyan indicates Chayote, red indicates border. For (c) and (d), cyan, green and yellow visualize asphalt, dirt, and sand roads, respectively (road types for illustration, not distinguished by the model).

not segment accurately. However, labeling of this class entailed a high degree of subjectivity. Despite the poor IoU the model still provided reasonable borders around its Chayote predictions (Fig. 6b). The mIoU and mean Dice coefficient (mDice) for Chayote excluding the border class were 0.889 and 0.939, respectively.

Merging predictions using the tile-crop strategy improved segmentation performance notably. Logit-merge scores (not shown here) were consistently lower than baseline scores. This proves the significance of post-processing geospatial predictions, which EcoMapper also facilitates.

Overall prediction quality was high: the generated segmentation maps were free of noise and incurred very few false positives. Moreover, models identified the main bodies of all feature clusters, as shown in Fig. 6. A closeup analysis of the difference between ground truth and prediction for Chayote is given in Fig. 7.

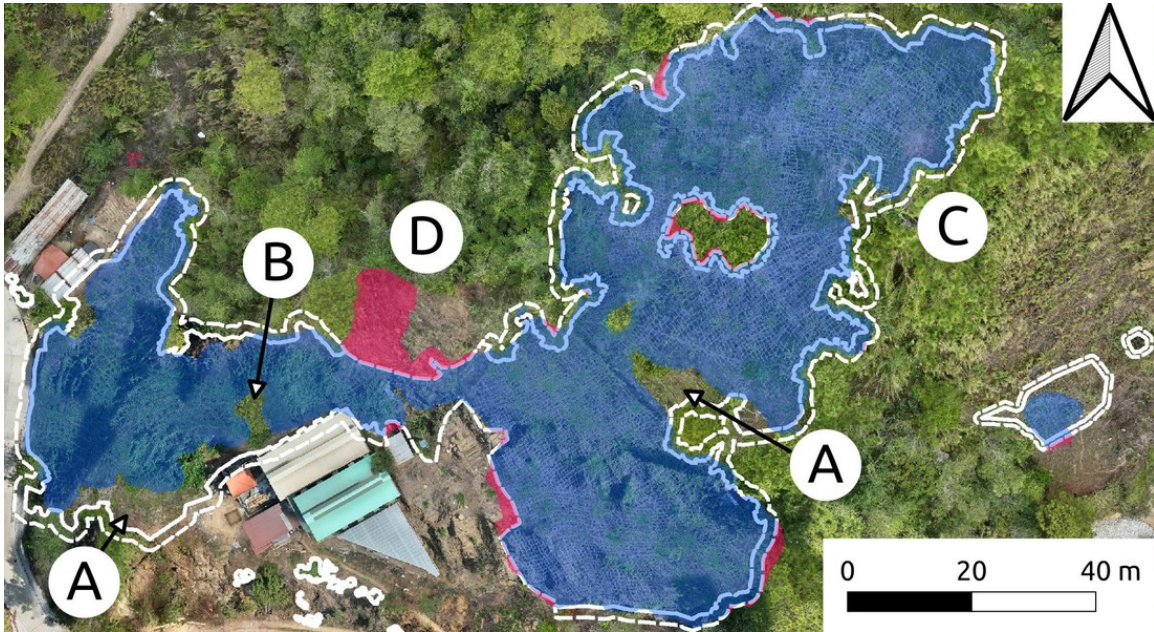


Figure 7: Closeup view of the difference between Chayote ground truth labels and predictions. Blue indicates agreement, red areas are false positives. White outline describes ground truth. (A) Largest disagreements occur in regions not containing Chayote, but contextually considered part of the plantation; (B) a species erroneously included in the ground truth is excluded by the model; (C) a large amount of disagreement is incurred at the boundary, as it is unclear during labeling where a plantation should end; (D) the largest false positive in the test dataset – it is still part of the main plantation and thus represents a sensible prediction, similar to the areas at (A).

3.3 Effects of survey characteristics on per-feature model performance

Fig. 8 visualizes model performance w.r.t. principal survey characteristics (GSD, feature size, dataset size). Corresponding tables are given in appendix K. An exemplary visualization of GSD impact on Chayote segmentation performance is given in appendix L.

While the Chayote model performed better at high resolutions, the performance dropped faster compared to the road model as GSD increased. As roads are generally easier to detect at coarser resolutions, the road model was robuster to changes in GSD, as illustrated by the slopes of the best fit lines. Beyond 0.5 m/px, the IoU for Chayote fell below the IoU for roads.

A sharp drop in Chayote performance was observed initially at 0.12 m/px. For roads, the performance was stable up to 0.12 m/px and then started to decrease slowly, but stabilized between 0.5 and 1 m/px before dropping sharply. As also observed in [21], segmentation performance sometimes improved when reducing GSD, which the results in Fig. 8 confirm.

Mean segmentation performance across degradation methods at 0.15 m/px was within 85.91% and 91.48% of the highest score for Chayote and roads, respectively. Findings thus suggest that VHR satellite products, such as super-resolution Maxar imagery, may provide a viable alternative to UAV imagery for VHR feature extraction.

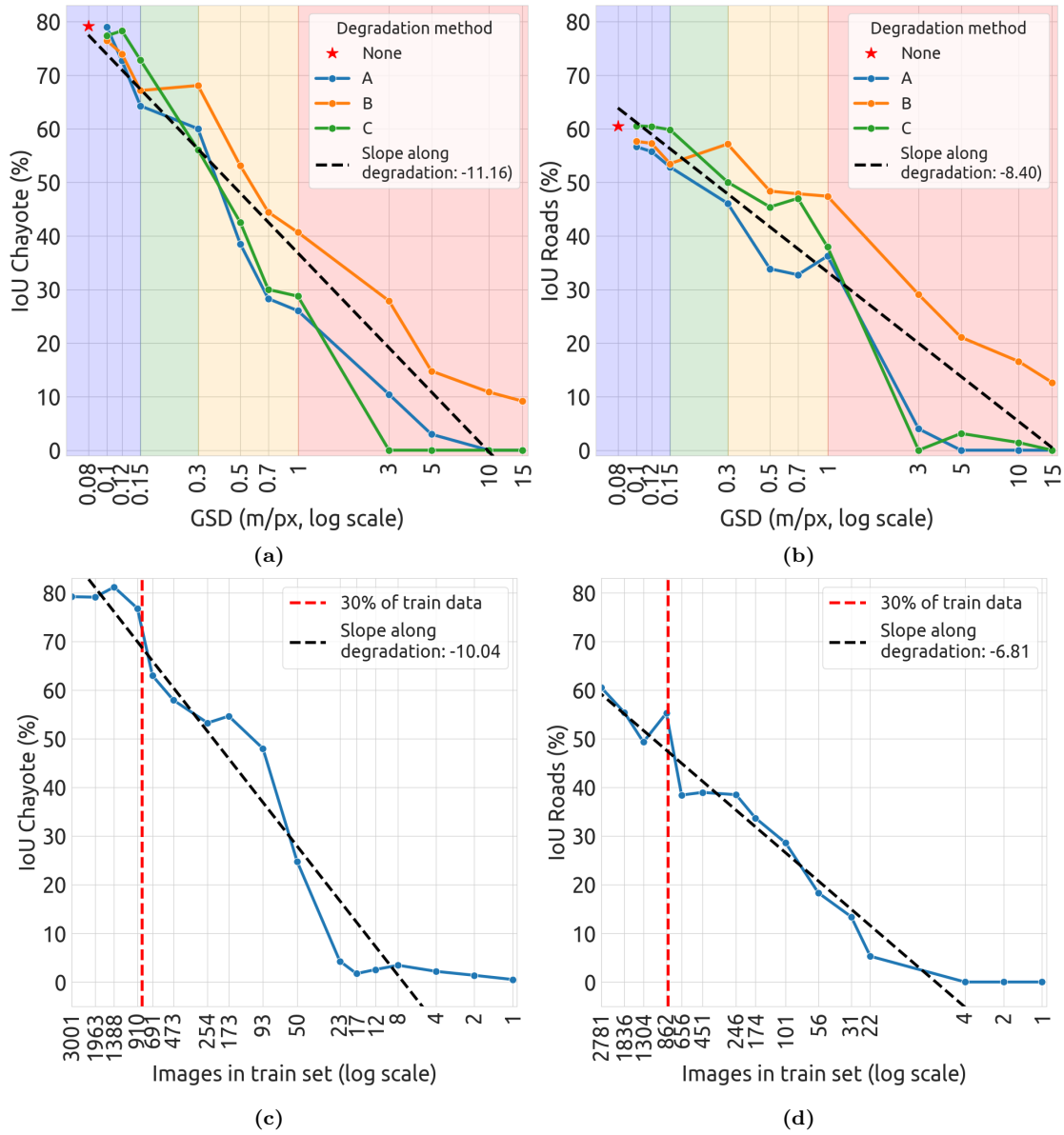


Figure 8: Chayote (a, c) and road (b, d) IoU model scores relative to GSD and dataset size. Slight differences in image counts in (c) and (d) are due to the difference in splits shown in Fig. 4. Background colors in (a) and (b) indicate which RS products provide the shown GSDs. Blue: UAVs; green: Maxar satellites with super-resolution post-processing; yellow: VHR commercial satellites; red: non-commercial satellites.

Dataset size also had a severe impact on model performance, visualized by the slopes of best fit lines. Model performance started to decline strongly when training on less than 30% of tiles from the original training set (indicated by red lines). The slope in Fig. 8c was again steeper compared to Fig. 8d, suggesting that more images are required to train a model on smaller features. The intermediate performance plateau in Fig. 8d is comparable to the plateau in Fig. 8b, and suggests that loss preceding the plateau stems from segmentation of smaller dirt roads. Larger asphalted roads are then segmented reliably until much stronger dataset degradations occur.

4 Discussion

4.1 EcoMapper did not require dataset-specific tuning to achieve strong segmentation performance

EcoMapper mIoU and mDice scores for Chayote and roads were comparable to other UAV-based studies using ViT networks; c.f. [53, 54, 55, 56] for studies of features comparable to Chayote, and [57, 58, 59, 60] for studies on roads and similar features.

All cited works designed their networks based on the dataset at hand. EcoMapper models were not tuned but their segmentation performance matched performance figures of prior studies. The first research objective to design a framework for arbitrary segmentation was thus achieved, without compromising on segmentation performance. Results show that transfer training of ViT networks represents a compelling alternative to redesigning models on a per-study basis.

4.2 Relationship between GSD and feature size

The results in Fig. 8 show that several GSDs allowed for accurate feature segmentation. It is desirable to identify the maximum GSD before performance deteriorates, to ensure that data collected in surveys are suitable for analysis with DL.

The Cording Index (CI) proposed below provides a lower and upper bound on the “critical GSD” at which model performance declines. Surveys may orient their choice of GSD based on this interval. The index was established from empirical study of the results in section 3, and from figures reported in prior works [30, 61].

1. Let F be the feature to identify.
2. Determine the smallest visible attribute (SVA) of F in overhead imagery that contributes to the uniqueness or identifiability of F .
3. Repeatedly measure the SVA size in various locations across the dataset. For rectangular shapes, measure the shorter side length. For circular shapes, measure the diameter. Highly irregular shapes cannot be measured directly; an average of the lengths of segments may be chosen, but first ensure the SVA was selected correctly.
4. Using the measurements, determine the upper and lower bounds of the SVA’s size, f_{s_1} and f_{s_2} .
5. The critical GSD for F is then suggested to lie in the following interval:

$$\text{GSD}_F \in \left(\frac{f_{s_1}}{3}, \frac{f_{s_2}}{3} \right) \quad (3)$$

CI aims to balance model performance and surveying duration. GSDs far below $\frac{f_{s_1}}{3}$ will thereafter not result in large performance gains. Conversely, GSDs far above $\frac{f_{s_2}}{3}$ will not offer the model sufficient information to identify F without incurring significant error.

Below it is shown that CI can be applied to obtain sensible GSD intervals for several features and models in this study and prior research.

4.2.1 GSD prediction for Chayote, roads, and other features

The SVA for Chayote are its leaves, which are heart-shaped and in the dataset had a diameter of 15–35 cm. Using CI, the critical GSD in m/px for this feature is in $(\frac{0.15}{3} = 0.05, \frac{0.35}{3} \approx 0.117)$. This interval is appropriate, as Chayote segmentation performance declined steadily beyond 0.10–0.12 m/px and improved marginally towards 0.08 m/px (c.f. Fig. 8).

Asphalted roads in the dataset lacked markings and had no other SVA. Their width ranged from 3–8 m. The SVA of smaller dirt roads were tire tracks, which distinguished them from farmland. Individually, these tracks were found to be approximately 0.4–0.85 m wide.

CI then gives $(\frac{0.4}{3} \approx 0.13, \frac{0.85}{3} \approx 0.28)$ as GSD interval in m/px for dirt roads. Reviewing Fig. 8, the performance was initially stable, confirming that GSDs below the lower bound did not significantly improve the model’s performance. In addition, performance started to deteriorate around 0.12–0.15 m/px, with a strong dip for all degradation methods from 0.3 m/px to 0.5 m/px. This indicates that most dirt roads in the dataset were very difficult to identify above 0.3 m/px, coinciding closely with the upper bound of CI.

Road segmentation performance stabilized from 0.3 to around 1 m/px, suggesting that large asphalted roads being were easily detectable in this GSD range. For asphalted roads, the GSD interval according to CI is $(\frac{3}{3} = 1, \frac{8}{3} \approx 2.67)$. This explains the drop in performance from 1 to 3 m/px, and the stable performance from 0.3–1 m/px.

In appendix M, additional applications of CI to other features from previous studies are made. CI provides sensible GSD intervals for these cases, even though different models and datasets were used.

4.3 Tradeoffs between survey characteristics and DL performance

CI can provide an optimal GSD range for a specific feature, to accelerate data collection without deteriorating model performance. However, sampling at maximum quality can make data more versatile for future analysis of small-scale features. A tradeoff between surveying resources, features to study, and model performance must therefore be made.

Surveying extent, simulated with dataset size, must also be considered. Based on Fig. 8 at least 30% of samples from the initial training set were needed to achieve adequate segmentation performance. Performance gains from using additional data were unclear.

Models may perform equally well with fewer training samples on a test set of the same study region. However, DL models generalize better when trained on more data points [62, 63]. If a model should be reapplied to other regions in the future, training on a larger dataset may prove beneficial. The scope of model application thus needs to be taken into account when choosing survey extent.

4.4 Proposal for an integrated DL-RS field survey workflow

A surveying workflow was developed from the studied effects of FSCs on DL performance. The workflow is illustrated in Fig. 9. Feature size, survey area, and GSD estimated by CI were integrated to balance the tradeoff between image resolution, survey resources, and DL performance.

Critically, additional survey adjustments may be needed to ensure sufficient data is collected. In case

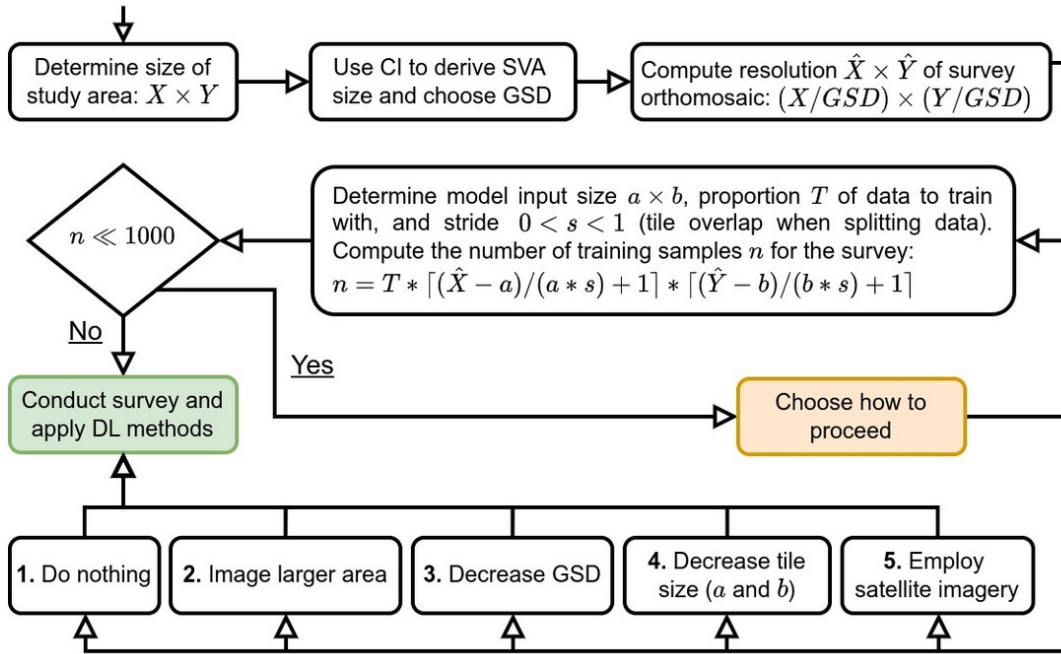


Figure 9: Field survey methodology with mechanisms to accommodate for DL model requirements. Survey feasibility is informed through study extent, feature size, GSD, and the number of training samples resulting from these characteristics. Actions are proposed for cases of data shortage, see text for details.

of data shortage, five possible actions with different implications on survey characteristics and model performance are proposed:

1. Do nothing: Survey duration is unaffected, but model performance may be impaired if the dataset is too small, due to overfitting (Figs. 8c and 8d).
2. Image larger area: Survey duration increases, but the model receives sufficient data at the desired GSD.
3. Decrease GSD (by reducing imaging altitude or using a higher fidelity sensor): Survey duration increases, the model receives enough data, but may perform suboptimally if unnecessary details are captured. Simultaneously, VHR imagery can be synthetically downsampled and allows for future analysis of smaller features. Exemplary implications of GSD on imaging extent and surveying duration are described in appendix N.
4. Reduce tile size: Survey duration is unaffected, the model receives sufficient samples, but smaller tiles may impact model performance.
5. Employ satellite data: Commercial VHR satellite products may present a viable alternative to UAV surveying, as demonstrated by model performance figures at 0.15 m/px in Fig. 8. However, satellite imagery can be noisier and occluded by clouds, thus performance figures from this UAV-based study may not directly translate to satellite use.

Future works should investigate the implications of outlined choices on model performance, and attempt to apply the proposed workflow together with EcoMapper for a comprehensive feature study.

5 Conclusion

This study proposed EcoMapper, a pipeline for segmentation of arbitrary features in RS imagery. Using EcoMapper, it was shown that two visually distinct features can be successfully segmented in a complex, real-world drone dataset.

Code profiling proved that EcoMapper achieves high computational performance in data processing and model training tasks. Segmentation performance without dataset-specific tuning was competitive with results of comparable studies which designed models for particular datasets. The proposed Coding Index and DL-informed workflow for RS surveys provide a foundation to understand and leverage the synergies of DL and RS, with the aim to accelerate field surveys and make data collection more effective.

EcoMapper predictions enable species specific analysis over the domain, such as shown in appendix O, thereby supporting systems of precision agriculture, estimation of biodiversity, and many more. Additional work is needed to lower computational requirements and encourage deployment of DL-based solutions on less powerful platforms. Future studies to segment RS imagery may apply EcoMapper to avoid the need for RS data processing and model implementation.

Funding

The authors acknowledge that they did not receive funding for this work.

Conflicts of Interest

The authors declare that there is no conflict of interest regarding the publication of this article.

References

- [1] Megan M. Coffey. ‘Balancing Privacy Rights and the Production of High-Quality Satellite Imagery’. In: *Environmental Science and Technology* 54.11 (May 2020), pp. 6453–6455. DOI: <https://doi.org/10.1021/acs.est.0c02365>.
- [2] G. A. Fotso Kamga et al. ‘Advancements in satellite image classification: methodologies, techniques, approaches and applications’. In: *International Journal of Remote Sensing* 42.20 (Sept. 2021), pp. 7662–7722. DOI: <https://doi.org/10.1080/01431161.2021.1954261>.
- [3] Asmae Dakir, Barramou Fatima Zahra and Alami Bachir Omar. ‘Optical satellite images services for precision agricultural use: a review’. In: *remote sensing* 4 (2021), p. 18. DOI: <https://doi.org/http://dx.doi.org/10.25046/aj060337>.
- [4] Ann E. McKellar, Nicholas G. Shephard and Dominique Chabot. ‘Dual visible-thermal camera approach facilitates drone surveys of Colonial Marshbirds’. In: *Remote Sensing in Ecology and Conservation* 7.2 (2020), pp. 214–226. DOI: <https://doi.org/10.1002/rse2.183>.
- [5] Francisco Javier Ancin-Murguzur et al. ‘Drones as a tool to monitor human impacts and vegetation changes in parks and protected areas’. In: *Remote Sensing in Ecology and Conservation* 6.1 (Sept. 2019). Ed. by Ned Horning and Anna Carter, pp. 105–113. DOI: <https://doi.org/10.1002/rse2.127>.
- [6] Elisa Casella et al. ‘Mapping coral reefs using consumer-grade drones and structure from motion photogrammetry techniques’. In: *Coral Reefs* 36.1 (Nov. 2016), pp. 269–275. DOI: <https://doi.org/10.1007/s00338-016-1522-0>.
- [7] Matheus Pinheiro Ferreira et al. ‘Individual tree detection and species classification of Amazonian palms using UAV images and deep learning’. In: *Forest Ecology and Management* 475 (Nov. 2020), p. 118397. DOI: <https://doi.org/10.1016/j.foreco.2020.118397>.
- [8] Teja Kattenborn et al. ‘Convolutional Neural Networks accurately predict cover fractions of plant species and communities in Unmanned Aerial Vehicle imagery’. In: *Remote Sensing in Ecology and Conservation* 6.4 (Feb. 2020). Ed. by Ned Horning and Nicola Clerici, pp. 472–486. DOI: <https://doi.org/10.1002/rse2.146>.
- [9] Bipul Neupane, Teerayut Horanont and Nguyen Duy Hung. ‘Deep learning based banana plant detection and counting using high-resolution red-green-blue (RGB) images collected from unmanned aerial vehicle (UAV)’. In: *PLOS ONE* 14.10 (Oct. 2019). Ed. by Krishna Prasad Vadrevu, e0223906. DOI: <https://doi.org/10.1371/journal.pone.0223906>.
- [10] Everton Castelão Tetila et al. ‘Automatic Recognition of Soybean Leaf Diseases Using UAV Images and Deep Convolutional Neural Networks’. In: *IEEE Geoscience and Remote Sensing Letters* 17.5 (2020), pp. 903–907. DOI: <https://doi.org/10.1109/LGRS.2019.2932385>.
- [11] Sylvain Jay et al. ‘Exploiting the centimeter resolution of UAV multispectral imagery to improve remote-sensing estimates of canopy structure and biochemistry in sugar beet crops’. In: *Remote Sensing of Environment* 231 (2019), p. 110898. ISSN: 0034-4257. DOI: <https://doi.org/10.1016/j.rse.2018.09.011>.

- [12] Liangpei Zhang, Lefei Zhang and Bo Du. ‘Deep Learning for Remote Sensing Data: A Technical Tutorial on the State of the Art’. In: *IEEE Geoscience and Remote Sensing Magazine* 4.2 (2016), pp. 22–40. DOI: <https://doi.org/10.1109/MGRS.2016.2540798>.
- [13] John E. Ball, Derek T. Anderson and Chee Seng Chan Sr. ‘Comprehensive survey of deep learning in remote sensing: theories, tools, and challenges for the community’. In: *Journal of Applied Remote Sensing* 11.4 (2017), p. 042609. DOI: <https://doi.org/10.1117/1.JRS.11.042609>.
- [14] Lei Ma et al. ‘Deep learning in remote sensing applications: A meta-analysis and review’. In: *ISPRS Journal of Photogrammetry and Remote Sensing* 152 (2019), pp. 166–177. ISSN: 0924-2716. DOI: <https://doi.org/10.1016/j.isprsjprs.2019.04.015>.
- [15] Rissouni Youssef, Moumen Aniss and Chao Jamal. ‘Machine Learning and Deep Learning in Remote Sensing and Urban Application: A Systematic Review and Meta-Analysis’. In: *Proceedings of the 4th Edition of International Conference on Geo-IT and Water Resources 2020, Geo-IT and Water Resources 2020*. GEOIT4W-2020. Al-Hoceima, Morocco: Association for Computing Machinery, 2020. ISBN: 9781450375788. DOI: <https://doi.org/10.1145/3399205.3399224>.
- [16] Sr Pielke Roger A., Rezaul Mahmood and Clive McAlpine. ‘Land’s complex role in climate change’. In: *Physics Today* 69.11 (Nov. 2016), pp. 40–46. ISSN: 0031-9228. DOI: <https://doi.org/10.1063/PT.3.3364>.
- [17] Benjamin Sleeter et al. *Chapter 5 : Land Cover and Land Use Change. Impacts, Risks, and Adaptation in the United States: The Fourth National Climate Assessment, Volume II*. Tech. rep. 2018. DOI: <https://doi.org/10.7930/nca4.2018.ch5>.
- [18] Yigal Elad and Ilaria Pertot. ‘Climate Change Impacts on Plant Pathogens and Plant Diseases’. In: *Journal of Crop Improvement* 28.1 (2014), pp. 99–139. DOI: <https://doi.org/10.1080/15427528.2014.865412>.
- [19] R. K. Mall et al. ‘Water resources and climate change: An Indian perspective’. In: *Current Science* 90.12 (2006), pp. 1610–1626. ISSN: 00113891. URL: <http://www.jstor.org/stable/24091910> (visited on 10/06/2023).
- [20] Dimosthenis C. Tsouros, Stamatia Bibi and Panagiotis G. Sarigiannidis. ‘A Review on UAV-Based Applications for Precision Agriculture’. In: *Information* 10.11 (Nov. 2019), p. 349. DOI: <https://doi.org/10.3390/info10110349>.
- [21] Jayme Garcia Arnal Barbedo et al. ‘A Study on the Detection of Cattle in UAV Images Using Deep Learning’. In: *Sensors* 19.24 (2019). ISSN: 1424-8220. DOI: <https://doi.org/10.3390/s19245436>.
- [22] Benjamin J. Heil et al. ‘Reproducibility standards for machine learning in the life sciences’. In: *Nature Methods* 18.10 (Oct. 2021), pp. 1132–1135. ISSN: 1548-7105. DOI: <https://doi.org/10.1038/s41592-021-01256-7>.

- [23] J. Machicao et al. ‘Mitigation Strategies to Improve Reproducibility of Poverty Estimations From Remote Sensing Images Using Deep Learning’. In: *Earth and Space Science* 9.8 (Aug. 2022). DOI: <https://doi.org/10.1029/2022ea002379>.
- [24] Md. Saif Hassan Onim et al. ‘LULC classification by semantic segmentation of satellite images using FastFCN’. In: *CoRR* abs/2011.06825 (Oct. 2020). DOI: <https://doi.org/10.48550/arXiv.2011.06825>.
- [25] Azavea/Element 84, Robert Cheetham. *Raster Vision: An open source library and framework for deep learning on satellite and aerial imagery*. Jan. 2023. DOI: <https://doi.org/10.5281/zenodo.8018177>.
- [26] Adam Paszke et al. ‘PyTorch: An Imperative Style, High-Performance Deep Learning Library’. In: *CoRR* abs/1912.01703 (2019). DOI: <https://doi.org/10.48550/arXiv.1912.01703>.
- [27] OpenMMLab. *MMSegmentation: OpenMMLab Semantic Segmentation Toolbox and Benchmark*. <https://github.com/open-mmlab/mms Segmentation>. 2023. (Visited on 24/07/2023).
- [28] Alexander Kirillov et al. ‘Segment Anything’. In: *arXiv:2304.02643* (2023).
- [29] Kaaviya Velumani et al. ‘Estimates of maize plant density from UAV RGB images using Faster-RCNN detection model: impact of the spatial resolution’. In: *Plant Phenomics* 2021 (2021). DOI: <https://doi.org/10.34133/2021/9824843>.
- [30] Jasper Brown et al. ‘Automated aerial animal detection when spatial resolution conditions are varied’. In: *Computers and Electronics in Agriculture* 193 (2022), p. 106689. ISSN: 0168-1699. DOI: <https://doi.org/10.1016/j.compag.2022.106689>.
- [31] Jonas Güttler, Julia Niebling and Xiao Xiang Zhu. ‘Analysing the Interactions Between Training Dataset Size, Label Noise and Model Performance in Remote Sensing Data’. In: *IGARSS 2022 - 2022 IEEE International Geoscience and Remote Sensing Symposium*. 2022, pp. 303–306. DOI: <https://doi.org/10.1109/IGARSS46834.2022.9884570>.
- [32] Zachary D. Calhoun et al. ‘Self-Supervised Encoders Are Better Transfer Learners in Remote Sensing Applications’. In: *Remote Sensing* 14.21 (2022). ISSN: 2072-4292. DOI: <https://doi.org/10.3390/rs14215500>.
- [33] QGIS Development Team. *QGIS Geographic Information System*. QGIS Association. 2023. URL: <https://www.qgis.org>.
- [34] CVAT.ai Corporation. *Computer Vision Annotation Tool (CVAT)*. Version 2.2.0. Sept. 2022. URL: <https://github.com/opencv/cvat>.
- [35] Sphinx. *The Sphinx documentation generator*. May 2023. URL: <https://github.com/sphinx-doc/sphinx> (visited on 22/07/2023).
- [36] Jazzband. 2023. URL: <https://github.com/jazzband/pip-tools> (visited on 24/07/2023).
- [37] Even Rouault et al. *GDAL*. 2023. DOI: <https://doi.org/https://doi.org/10.5281/ZENODO.5884351>.
- [38] Anaconda. *Anaconda Software Distribution*. <https://www.anaconda.com/>. July 2023. (Visited on 22/07/2023).

- [39] OpenMMLab. 2023. URL: <https://openmmlab.com/> (visited on 27/08/2023).
- [40] Seunghan Park et al. *MultiEarth 2023 Deforestation Challenge – Team FOREVER*. 2023. arXiv: [2306.11762](https://arxiv.org/abs/2306.11762) [cs.CV].
- [41] Wenwei Zhang et al. *K-Net: Towards Unified Image Segmentation*. 2021. arXiv: [2106.14855](https://arxiv.org/abs/2106.14855) [cs.CV].
- [42] Chen Liang et al. *GMMSeg: Gaussian Mixture based Generative Semantic Segmentation Models*. 2022. arXiv: [2210.02025](https://arxiv.org/abs/2210.02025) [cs.CV].
- [43] Alexander Buslaev et al. ‘Albumentations: Fast and Flexible Image Augmentations’. In: *Information* 11.2 (2020). ISSN: 2078-2489. DOI: <https://doi.org/10.3390/info11020125>.
- [44] Alex Krizhevsky, Ilya Sutskever and Geoffrey E. Hinton. ‘ImageNet Classification with Deep Convolutional Neural Networks’. In: *Commun. ACM* 60.6 (May 2017), pp. 84–90. ISSN: 0001-0782. DOI: <https://doi.org/10.1145/3065386>.
- [45] Agnieszka Mikołajczyk and Michał Grochowski. ‘Data augmentation for improving deep learning in image classification problem’. In: *2018 International Interdisciplinary PhD Workshop (IIPHDW)*. 2018, pp. 117–122. DOI: <https://doi.org/10.1109/IIPHDW.2018.8388338>.
- [46] Connor Shorten and Taghi M Khoshgoftaar. ‘A survey on image data augmentation for deep learning’. In: *Journal of big data* 6.1 (2019), pp. 1–48.
- [47] N. Karasiak et al. ‘Spatial dependence between training and test sets: another pitfall of classification accuracy assessment in remote sensing’. In: *Machine Learning* 111.7 (Apr. 2021), pp. 2715–2740. DOI: <https://doi.org/10.1007/s10994-021-05972-1>.
- [48] Bowen Cheng et al. ‘Masked-attention Mask Transformer for Universal Image Segmentation’. In: 2022. DOI: <https://doi.org/10.48550/arXiv.2112.01527>.
- [49] Marius Cordts et al. ‘The Cityscapes Dataset for Semantic Urban Scene Understanding’. In: *CoRR* abs/1604.01685 (2016). arXiv: [1604.01685](https://arxiv.org/abs/1604.01685). URL: <http://arxiv.org/abs/1604.01685>.
- [50] Bolei Zhou et al. ‘Scene Parsing through ADE20K Dataset’. In: *2017 IEEE Conference on Computer Vision and Pattern Recognition (CVPR)*. 2017, pp. 5122–5130. DOI: <https://doi.org/10.1109/CVPR.2017.544>.
- [51] Ze Liu et al. *Swin Transformer: Hierarchical Vision Transformer using Shifted Windows*. 2021. arXiv: [2103.14030](https://arxiv.org/abs/2103.14030) [cs.CV].
- [52] Ilya Loshchilov and Frank Hutter. *Decoupled Weight Decay Regularization*. 2019. arXiv: [1711.05101](https://arxiv.org/abs/1711.05101) [cs.LG].
- [53] Chengquan Zhou et al. ‘An automated, high-performance approach for detecting and characterizing broccoli based on UAV remote-sensing and transformers: A case study from Haining, China’. In: *International Journal of Applied Earth Observation and Geoinformation* 114 (2022), p. 103055. ISSN: 1569-8432. DOI: <https://doi.org/10.1016/j.jag.2022.103055>.
- [54] Felipe David Georges Gomes et al. ‘Urban Trees Mapping Using Multi-Scale Rgb Image and Deep Learning Vision Transformer-Based’. In: *SSRN Electronic Journal* (2022). DOI: <https://doi.org/10.2139/ssrn.4167085>.

- [55] Mohamed Barakat A. Gibril et al. ‘Large-Scale Date Palm Tree Segmentation from Multiscale UAV-Based and Aerial Images Using Deep Vision Transformers’. In: *Drones* 7.2 (2023). ISSN: 2504-446X. DOI: <https://doi.org/10.3390/drones7020093>.
- [56] Haozhe Huang et al. ‘AMDNet: A Modern UAV RGB Remote-Sensing Tree Species Image Segmentation Model Based on Dual-Attention Residual and Structure Re-Parameterization’. In: *Forests* 14.3 (2023). ISSN: 1999-4907. DOI: <https://doi.org/10.3390/f14030549>.
- [57] Libo Wang et al. ‘Building Extraction With Vision Transformer’. In: *IEEE Transactions on Geoscience and Remote Sensing* 60 (2022), pp. 1–11. DOI: <https://doi.org/10.1109/TGRS.2022.3186634>.
- [58] Zheng Zhang et al. ‘DCS-TransUpperNet: Road Segmentation Network Based on CSwin Transformer with Dual Resolution’. In: *Applied Sciences* 12.7 (2022). ISSN: 2076-3417. DOI: <https://doi.org/10.3390/app12073511>.
- [59] Satyawant Kumar, Abhishek Kumar and Dong-Gyu Lee. In: *Mathematics* 10.24 (2022). ISSN: 2227-7390. DOI: <https://doi.org/10.3390/math10244735>.
- [60] Xingjian Gu et al. ‘Adaptive enhanced swin transformer with U-net for remote sensing image segmentation’. In: *Computers and Electrical Engineering* 102 (2022), p. 108223. ISSN: 0045-7906. DOI: <https://doi.org/10.1016/j.compeleceng.2022.108223>.
- [61] Osman Ilniyaz, Alishir Kurban and Qingyun Du. ‘Leaf Area Index Estimation of Pergola-Trained Vineyards in Arid Regions Based on UAV RGB and Multispectral Data Using Machine Learning Methods’. In: *Remote Sensing* 14.2 (2022). ISSN: 2072-4292. DOI: <https://doi.org/10.3390/rs14020415>.
- [62] Jayme Garcia Arnal Barbedo. ‘Impact of dataset size and variety on the effectiveness of deep learning and transfer learning for plant disease classification’. In: *Computers and Electronics in Agriculture* 153 (2018), pp. 46–53. ISSN: 0168-1699. DOI: <https://doi.org/10.1016/j.compag.2018.08.013>.
- [63] Deepak Soekhoe, Peter van der Putten and Aske Plaat. ‘On the Impact of Data Set Size in Transfer Learning Using Deep Neural Networks’. In: *Advances in Intelligent Data Analysis XV*. Ed. by Henrik Boström et al. Cham: Springer International Publishing, 2016, pp. 50–60.
- [64] G. Bradski. ‘The OpenCV Library’. In: *Dr. Dobb’s Journal of Software Tools* (2000).
- [65] Ashish Vaswani et al. *Attention Is All You Need*. 2023. arXiv: [1706.03762](https://arxiv.org/abs/1706.03762) [cs.CL].
- [66] Alexey Dosovitskiy et al. ‘An Image is Worth 16x16 Words: Transformers for Image Recognition at Scale’. In: *CoRR* abs/2010.11929 (2020). arXiv: [2010.11929](https://arxiv.org/abs/2010.11929). URL: <https://arxiv.org/abs/2010.11929>.
- [67] Robin Strudel et al. *Segformer: Transformer for Semantic Segmentation*. 2021. arXiv: [2105.05633](https://arxiv.org/abs/2105.05633) [cs.CV].
- [68] Sixiao Zheng et al. *Rethinking Semantic Segmentation from a Sequence-to-Sequence Perspective with Transformers*. 2021. arXiv: [2012.15840](https://arxiv.org/abs/2012.15840) [cs.CV].

- [69] Bowen Cheng, Alexander G. Schwing and Alexander Kirillov. *Per-Pixel Classification is Not All You Need for Semantic Segmentation*. 2021. arXiv: [2107.06278](https://arxiv.org/abs/2107.06278) [cs.CV].
- [70] Native Plant Trust. *Vitis vinifera* — *European grape*. URL: <https://gobotany.nativeplanttrust.org/species/vitis/vinifera/> (visited on 24/08/2023).
- [71] North Carolina Extension Gardener Plant Toolbox. *Vitis vinifera*. URL: <https://plants.ces.ncsu.edu/plants/vitis-vinifera/> (visited on 24/08/2023).
- [72] J. O. L Cerqueira et al. ‘Relationship between Zoometric Measurements in Holstein-Friesian Cow and Cubicle Size in Dairy Farms’. In: *International Journal of Morphology* 31.1 (Mar. 2013), pp. 55–63. DOI: <https://doi.org/10.4067/s0717-95022013000100008>.
- [73] Alexis Santana. *Black Angus Cattle Dimensions and Drawings*. Nov. 2022. URL: <https://www.dimensions.com/element/black-angus-cattle>.
- [74] Alexis Santana. *Holstein Friesian Cattle Dimensions and Drawings*. Nov. 2022. URL: <https://www.dimensions.com/element/holstein-friesian-cattle>.
- [75] Ontario. *Dairy cow comfort: tie-stall dimensions*. Aug. 2022. URL: <https://www.ontario.ca/page/dairy-cow-comfort-tie-stall-dimensions>.
- [76] Derick Omondi. *Domestic Sheep (Ovis aries)*. Nov. 2022. URL: <https://www.dimensions.com/element/domestic-sheep-ovis-aries>.

A Application of the Segment Anything Model (SAM) to a section of the Sto. Niño dataset

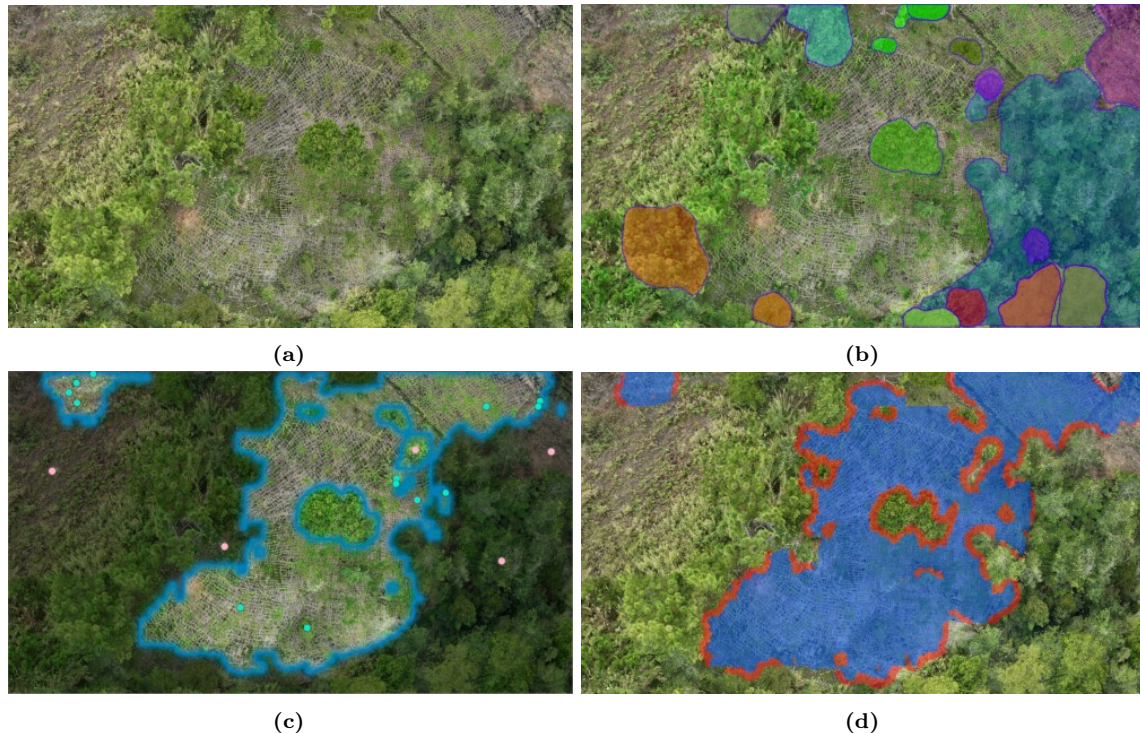


Figure A.1: Application of SAM to a Chayote plantation from the test portion of the Sto. Niño dataset. (a) Input image; (b) SAM segmentation in automatic mode; (c) SAM segmentation after 18 adjustment clicks by the user; (d) automatic segmentation by the model trained with EcoMapper (blue indicates Chayote, red border indicates model uncertainty).

The Segment Anything model (SAM) is part of Meta’s Segment Anything project [28], which consists of several novel segmentation tasks, a new dataset for segmentation containing 11M images and 1.1B masks, and SAM itself. SAM is a zero-shot network which extracts segmentation masks from images under a given task at interactive speed. Meta has made the model available for several tasks in an online demo, which allows users to segment objects over a large collection of images. A section of the Sto. Niño dataset was uploaded to this demo, showing a Chayote plantation and its surroundings, and the two main segmentation tasks of SAM were run on this image. Fig. A.1 illustrates the experiment, and compares the result with the predictions of a model trained by EcoMapper. Note that the image is part of the test set, i.e., it was not shown to the model during training.

B Overview of the Sto. Niño dataset



Figure B.2: An excerpt of the Sto. Niño dataset, showing large varieties of vegetation, infrastructure, and image quality. The native resolution of around 2cm/px remains fixed over the entire dataset.

C Labeling tutorials for QGIS and CVAT

The first tutorial series² details the labeling process in QGIS. It first walks through importing the dataset and creating image pyramids for accelerated navigation within the software. Then, the various labeling tools are showcased. Finally, the export process is detailed to generate segmentation maps in GeoTiff format.

Readers can also refer to an alternative tutorial³ for using the CVAT labeling tool, which partially automates label creation. This video explains how to first generate image tiles with EcoMapper, upload them to CVAT for labeling, and finally import the generated labels back into EcoMapper.

D View of a Chayote plantation in the Sto. Niño dataset



Figure D.3: A partial view of a Chayote plantation in the Tublay region. The trellises on which the fruits grow form a distinct grid-like shape when viewed from above.

²https://www.youtube.com/playlist?list=PLpVXG8nYO_inhvIa8aV7kWRqr4RjWe5BU

³<https://youtu.be/LK6WaPUBm08>

E EcoMapper Task Network

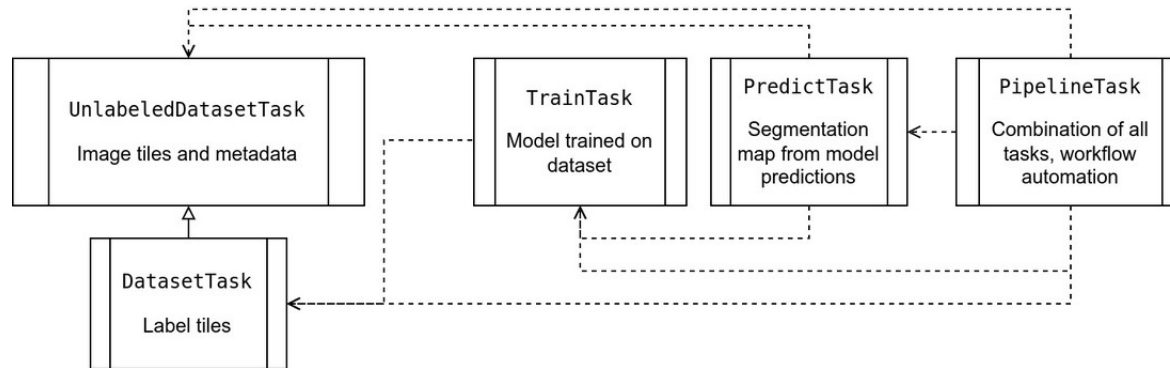


Figure E.4: The EcoMapper network of Tasks, using UML notation. **DatasetTask** inherits from **UnlabeledDatasetTask** to introduce labels. Dashed arrows indicate dependencies.

F Notable features of EcoMapper

F.1 Parallelized processing of large inputs

Data processing in EcoMapper was parallelized using Python's `concurrent.futures` module. The contained `ProcessPoolExecutor` creates a process for each job to run, instead of using threads. This allows side-stepping the global interpreter lock in Python which otherwise prevents multiple threads from executing Python byte code simultaneously. EcoMapper also chunks input data in advance to distribute the workload effectively across all cores. Inputs of arbitrary size are handled by using memory mapping.

F.2 Failsafes through journaling

Data processing and model training tasks run for long durations and can be interrupted due to power outages or unexpected resource constraints. EcoMapper atomically commits the progress of Tasks to a journal, which is read when restarting after an interruption. This allows the pipeline to continue computation from the last stable state.

F.3 Hardware compatibility

EcoMapper interfaces with the PyTorch training backend to allow training on a wide range of hardware configurations. The code has been tested on CPU-only systems, consumer-grade systems with a single GPU, as well as HPC environments with up to 8 GPUs. Computational requirements for training are adjustable by selecting a particular model variant during model selection, providing trade-offs between training cost and prediction quality.

F.4 Supported data formats and CVAT integration

The image and label map inputs to EcoMapper can have any common format, and in particular geospatial formats such as GeoTiff for images and GeoJSON and Shapefiles for label maps are supported. EcoMapper also supports reading annotations generated with CVAT to help accelerate the labeling procedure.

G Strategies for processing geospatial data in a DL context

G.1 Calculating sample weights for training

Algorithm G.1 Calculation of sample weights for the train dataset. Samples containing minority classes are weighted more strongly, and thus have higher probability of being drawn when a batch of training data is created.

Require: train_dataset_label_tiles

```
1: class_occurrences ← An empty list of lists
2: for label_tile in train_dataset_label_tiles do
3:    $m \leftarrow$  Load label_tile as a grayscale image ▷ Value of each pixel in  $m$  is its class
4:   Append the number of occurrences of each class in  $m$  to class_occurrences
5: end for
6: total_class_occurrences ← Sum of lists in class_occurrences

7: sample_weights ← Empty list
8: for sample_class_occurrences in class_occurrences do
9:    $s \leftarrow$  An empty list
10:  for  $i$ , class_occurrence in enumerate(sample_class_occurrences) do
11:    Append class_occurrence / total_class_occurrences[ $i$ ] to  $s$ 
▷ Proportion of class  $i$  in this tile, relative to proportion of  $i$  in dataset
12:  end for
13:  Append the sum of items in  $s$  to sample_weights
14: end for
15: return sample_weights
```

G.2 Merging predictions on model logits

The trained model generates per-pixel predictions for each image tile it is given. Unprocessed, such predictions are referred to as logits, which are “confidence scores” of the model to assign a pixel to a given class. Each image tile has an associated logit tile after predictions are completed. Due to tile overlap, these predictions cannot be stitched together into a segmentation map directly.

Let L denote the set of logit tiles overlapping at a pixel p , and T the set of image tiles corresponding to L . A logit tile $l_t \in L$, corresponding to image tile $t \in T$, has shape $(h, w, |C|)$, where h, w are the tile dimensions, and C the set of classes in the dataset. $l_t[p][c]$ (short for $l_t[p_y][p_x][c]$) indicates the model’s confidence that p in tile t belongs to class $c \in C$.

Then the class c_p of p in the merged segmentation map can be given by:

$$c_p = \arg \max_{c \in C} \left(\max_{t \in T} l_t[p][c] \right). \tag{G.1}$$

In other words, c_p maximizes the maximum logit over all tiles overlapping at p .

G.3 Merging predictions by cropping tiles

An alternative approach that is faster and yields higher quality results is to crop tiles by half the overlap factor (stride) along each side of the tile. Intuitively, the model has the most information about objects in the center of a tile. The further towards the border an object lies, the more likely it is to be cut off and not be identified accurately.

Programmatically, the cropping approach is faster because it can utilize vectorized array slicing operations to copy large chunks of each tile into the final segmentation map, whereas the previous approach performs per-pixel operations in plain Python code, making it orders of magnitude slower. Moreover, model confidence as expressed through logits can be noisy or erroneous, and may therefore not be the best merging criteria, particularly when the model is under-trained. Fig. G.5 illustrates these differences with an example.

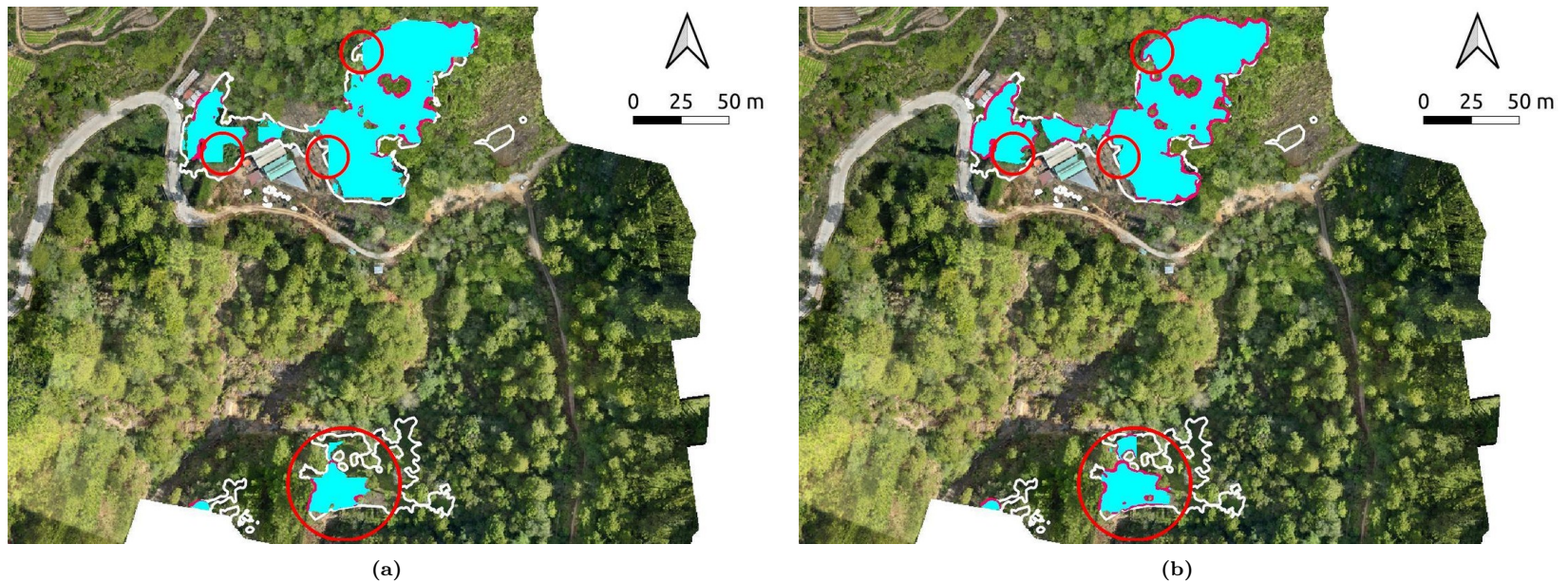


Figure G.5: Comparison of max-logit merging (a) vs tile-crop merging (b) for Chayote predictions at 0.3 m/px. Merging by cropping reduces artifacts and substantially increases the border size. Red circles indicate locations where the improvement is particularly visible.

H Overview of resolutions

Table H.1: Sto. Niño dataset resolutions and matching platforms

GSD	Resolution (W)	Resolution (H)	Platform
0.08	23662	25228	UAV
0.10	18930	20182	UAV
0.12	15775	16819	UAV
0.15	12620	13455	Maxar (Upscaled)
0.30	6310	6727	Maxar, Digital Globe
0.50	3786	4036	Maxar, Airbus
0.70	2704	2883	Maxar, Planet, CNES, KARI
1	1893	2018	Lockheed Martin Space
3	631	673	Planet
5	379	404	RapidEye Blackbridge
10	189	202	Sentinel-2
15	126	135	Landsat

I Detailed discussion of degradation methods

The degradation methods of this study were illustrated in Fig. 3. Method A downscales images and labels during training before they are aggregated into a mini-batch. This reduces the amount of information per input to the model, while maintaining pixel density, thus each pixel represents a larger physical distance. It also requires a different model architecture to accommodate for the new input size, which makes comparisons to the baseline more difficult. Downscaling of labels reduces the precision of gradient computations when updating model weights, which impedes training progress at low resolutions. `INTER_AREA` interpolation of the OpenCV library [64] was used for downscaling.

Pixelation (method B) does not affect input size, but also reduces the amount of conveyed information, while lowering pixel density. Unlike method A, labels are not degraded, which gives a better estimate of how image quality alone affects predictions. Method B represents a synthetic study of resolution degradation, as multiple pixels in the final tile represent a single pixel in the downsized tile. `INTER_AREA` interpolation was again used for downscaling, followed by bicubic upscaling.

Method C creates tiles which are “zoomed out” compared to the original input [21]. Detailed information at the pixel level is lost, but the model also receives a larger view of the surrounding area. The pixel density in this approach is unaffected, and each pixel covers a larger spatial distance. Most importantly, method C accurately simulates the change per tile when the satellite or drone capturing the imagery has higher altitude or is equipped with a sensor registering fewer samples. However, as the resolution of the orthomosaic is lowered, fewer tiles can be produced. This reduction in training data can affect model performance and lead to overfitting, and is investigated in detail in section 3. Each degraded dataset was generated by downscaling the original dataset using lanczos interpolation in QGIS [33].

J Mask2Former

Several prerequisites are needed to understand transformer networks, as they build on years of research into natural language processing (NLP) and input encoding. For brevity, only a brief overview is provided here, but readers are encouraged to refer to both the original paper on transformers, “Attention is all you need” [65], as well the excellent video series “StatQuest” by Josh Starmer⁴.

J.1 Transformer neural networks and the self attention mechanism

The transformer architecture is proving to outperform all previous approaches in NLP, computer vision (CV), data generation, and more. Its strong performance is not attributed to smart design choices in model architecture, though. In fact, the transformer is a far more general model than CNNs, LSTMs, and even MLPs.

Prior model architectures across domains heavily relied on inductive biases. Such biases tell the model *how* to tackle a task, and through training the model becomes better at applying the prescribed technique to the data, be it convolutions for image analysis, long short-term memory for text prediction, etc. Crucially, because the methodology is already defined, far less training data is needed for the model to converge to a trained state.

In contrast, the transformer architecture does not specify how a task should be solved. Inputs to the model are encoded to register their semantic meaning and position in the sequence, and using a mechanism called self-attention, the similarity between a sequence token to itself and all other tokens is computed. This self attention computation is quadratic in runtime, but can be computed in parallel for all tokens, which makes transformers far more computationally efficient than previous architectures.

However, the strong reduction in inductive biases require an abundance of training data for the model to converge. Not only must relationships in the data be identified by the model, but analysis techniques must first be learned. By allowing the model to develop its own methodology, with enough training data and time it can derive approaches that outperform “fixed” architectures like CNNs. Interestingly, it was shown that transformers could independently develop techniques akin to CNN convolution for CV tasks, and hierarchical analysis of grammar, context, and meaning in NLP tasks.

Conventional model architectures will still retain relevance whenever computational requirements or data availability are constrained. For the same reason, many popular transformer implementations are first pretrained on large generic datasets, such as ImageNet, to allow transfer training of models to specific tasks with fewer computational resources.

J.2 Vision transformers

The vision transformer (ViT) was first proposed in 2020 [66]. At the time, transformers in computer vision (CV) were employed by combining parts of their model architecture with CNNs. This is because self attention is prohibitively expensive to compute already for long text sequences, but images typically contain orders of magnitude more data points than text.

⁴<https://www.youtube.com/watch?v=zxQyTK8quyY>

The authors in [66] proposed a “pure” transformer architecture for CV. They solved the computational issue of self attention on images by first dividing the input image into so-called patches of 16x16. Using a linear transformation, each patch (unrolled to a 1-d vector) is projected into a lower dimensional space, and the resulting vector is positionally embedded, producing a patch embedding. Patch embeddings are then fed to a regular transformer. Learnable [class] embeddings are fed into the transformer encoder as the final inputs of the sequence, to produce an output that is fed to an MLP head for image classification.

The ViT architecture therefore solves the computational overhead of self attending to images, while still benefiting from the parallelization capabilities of transformers. This enabled the authors to train their ViT on orders of magnitude more data, and outperform all prior CNN-based approaches.

J.3 MaskFormer and Mask2Former

Semantic segmentation tasks, regardless of model architecture, were largely tackled as per-pixel classification problems. With the introduction of ViTs, works such as [67] and [68] demonstrated pixel-level semantic segmentation using transformer encoders and custom decoders that upsample the encoded input and transform it into the segmentation result.

However, pixel-level segmentation is not the only approach to semantic segmentation. Mask classification is an alternative approach where the model produces a number of segmentation masks for the same image, with each mask having a single class ID. While this enables semantic segmentation, it also allows for instance segmentation, where objects within the same class are distinguished.

MaskFormer [69] was introduced as the first ViT model to use mask classification for image segmentation. Its architecture naturally allows for semantic and instance segmentation. Moreover, models performing per-pixel semantic segmentation can be converted to the MaskFormer architecture, because MaskFormer uses a pixel-level module to generate feature maps from input images.

Mask2Former [48] later followed to improve upon the MaskFormer architecture. Its main difference is the use of masked attention, where unlike a regular transformer decoder used in MaskFormer, the decoder is restricted to focus on areas near predicted segments. Further, memory usage was optimized by computing loss over a set of randomly selected points, rather than entire predictions.

K Numeric data on per-feature model performance relative to survey characteristics

Table K.2: Quantative evaluation of Chayote segmentation performance as GSD is increased

Method	GSD (m/px)	mIoU	mDice	IoU Background	IoU Chayote	IoU Border	Best val. iteration
n/a	0.08	66.79	74.83	98.64	79.2	22.53	14500
A	0.10	67.13	75.34	98.64	78.94	23.81	6500
	0.12	64.85	73.84	98.24	72.67	23.65	2500
	0.15	58.89	67.56	97.73	64.24	14.68	18500
	0.30	55.94	64.22	97.39	59.98	10.53	11500
	0.50	46.80	54.80	96.23	38.47	5.69	16500
	0.70	42.07	49.53	93.96	28.28	3.96	7500
	1	41.79	49.36	94.23	26.02	5.13	11500
	3	34.43	38.39	92.86	10.43	0	6500
	5	32.37	34.25	94.12	2.98	0	19000
	10	31.47	32.37	94.4	0	0	500
15	31.5	32.39	94.5	0	0	500	
B	0.10	64.68	72.7	98.36	76.42	19.26	13500
	0.12	63.80	72.09	98.34	73.95	19.11	18000
	0.15	60.84	69.72	97.84	67.10	17.60	21500
	0.30	61.31	70.11	97.97	68.04	17.92	8500
	0.50	54.75	64.18	97.11	53.07	14.07	13000
	0.70	50.59	59.76	96.52	44.42	10.82	11500
	1	48.84	57.85	96.15	40.65	9.72	7500
	3	42.17	49.53	94.59	27.86	4.05	11500
	5	35.77	40.71	92.34	14.78	0.19	11500
	10	33.16	38.05	88.19	10.85	0.43	15500
15	32.66	9.16	88.83	9.16	0	13500	
C	0.10	65.78	73.97	98.46	77.33	212.56	8500
	0.12	65.62	73.48	98.60	78.24	20.02	6500
	0.15	64.11	72.81	98.34	72.79	21.21	2500
	0.30	56.73	66.34	97.6	56.04	16.54	1528
	0.50	50.66	60.12	96.96	42.49	12.53	630
	0.70	42.56	49.26	95.76	29.99	1.94	342
	1	42.44	48.88	96.74	28.73	1.86	90
	3	32.99	33.16	98.97	0	0	10
	5	33.21	33.27	99.64	0	0	6
	10	33.3	33.32	99.91	0	0	5
15	33.32	33.33	99.96	0	0	3	

Table K.3: Quantative evaluation of road segmentation performance as GSD is increased

Method	GSD (m/px)	mIoU	mDice	IoU Background	IoU Roads	Best val. iteration
n/a	0.08	79.84	87.49	99.16	60.52	5000
A	0.10	77.85	85.92	99.08	56.62	3000
	0.12	77.39	85.54	99.08	55.71	9000
	0.15	75.92	84.32	98.99	52.84	14000
	0.3	72.47	81.25	98.87	46.07	2000
	0.5	66.21	74.93	98.57	33.85	9000
	0.7	65.59	74.27	98.44	32.73	9000
	1	67.36	76.21	98.51	36.21	4000
	3	51.01	53.34	98.03	3.99	15000
	5	49.05	49.52	98.09	0.00	500
	10	48.95	49.47	97.90	0.00	500
B	0.10	78.35	86.32	99.09	57.61	3000
	0.12	78.18	86.18	99.11	57.25	3000
	0.15	76.24	84.59	99.02	53.46	3000
	0.3	78.10	86.12	99.09	57.12	3500
	0.5	73.64	82.32	98.95	48.34	16500
	0.7	73.40	82.10	98.92	47.84	4000
	1	73.10	81.86	98.82	47.39	4000
	3	63.75	72.12	98.45	29.05	4000
	5	59.69	66.98	98.31	21.08	22500
	10	57.19	63.67	97.80	16.58	15500
C	0.10	79.86	87.50	99.20	60.52	6500
	0.12	79.77	87.44	99.15	60.38	2500
	0.15	79.50	87.22	99.21	59.79	2500
	0.3	74.57	83.13	99.12	50.03	1146
	0.5	72.21	80.98	99.04	45.38	140
	0.7	72.99	81.72	99.00	46.99	152
	1	68.45	77.24	98.97	37.93	54
	3	49.83	49.92	99.66	0.00	2
	5	49.79	52.13	96.45	3.13	7
	10	50.64	51.38	99.84	1.44	8
15	50.00	50.00	99.99	0.00	1	

Table K.4: Quantative evaluation of feature segmentation performance as train dataset size is decreased

Feature	Tiles in Train Set	mIoU	mDice	IoU Background	IoU Feature	IoU Border
Chayote	3001	66.79	74.83	98.64	79.2	22.53
	1963	67.52	75.81	98.65	79.1	24.82
	1388	68.34	76.37	98.71	81.18	25.11
	910	65.55	73.81	98.36	76.81	21.49
	254	56.68	67.02	96.93	53.25	19.85
	93	55.31	66.03	96.86	47.99	21.09
	50	41.69	48.94	95.31	24.79	4.97
	23	32.37	34.93	92.61	4.28	0.21
	2	28.67	31.66	84.21	1.37	0.43
	1	31.03	32.39	92.55	0.51	0.01
Roads	2781	79.84	87.49	99.16	60.52	n/a
	1836	77.26	85.43	99.12	55.39	n/a
	1304	74.17	82.78	99.01	49.32	n/a
	862	77.2	85.38	99.12	55.28	n/a
	246	68.57	77.46	98.65	38.5	n/a
	101	63.58	71.88	98.56	28.6	n/a
	56	58.34	59.85	98.37	18.32	n/a
	31	55.8	61.37	98.19	13.41	n/a
	4	49.08	49.54	98.17	0	n/a
	1	49.08	49.54	98.17	0	n/a

L Degradation visualization

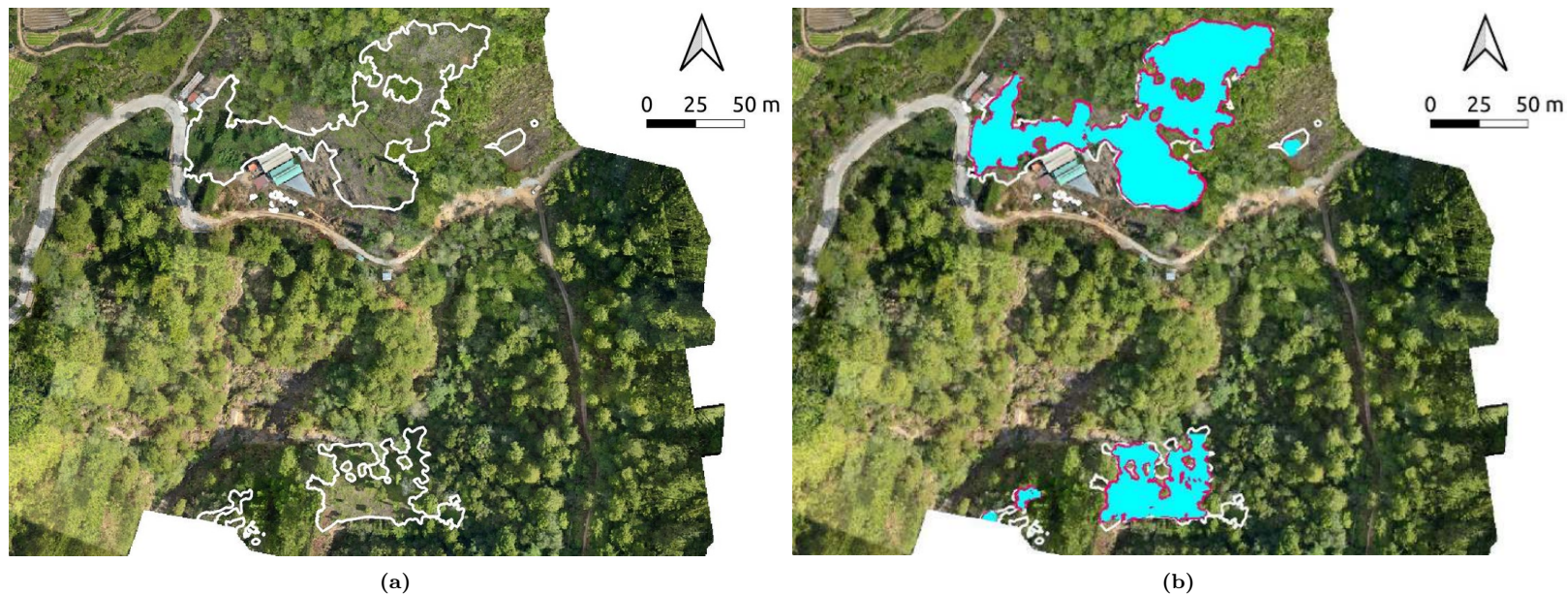


Figure L.6: Setup for visualization of performance degradation for Chayote w.r.t. GSD. (a) Ground truth Chayote labels (border merged); and (b) model prediction at 8cm/px. Cyan and red indicate predicted Chayote and border, respectively. See Fig. L.7 for degradation over each method.

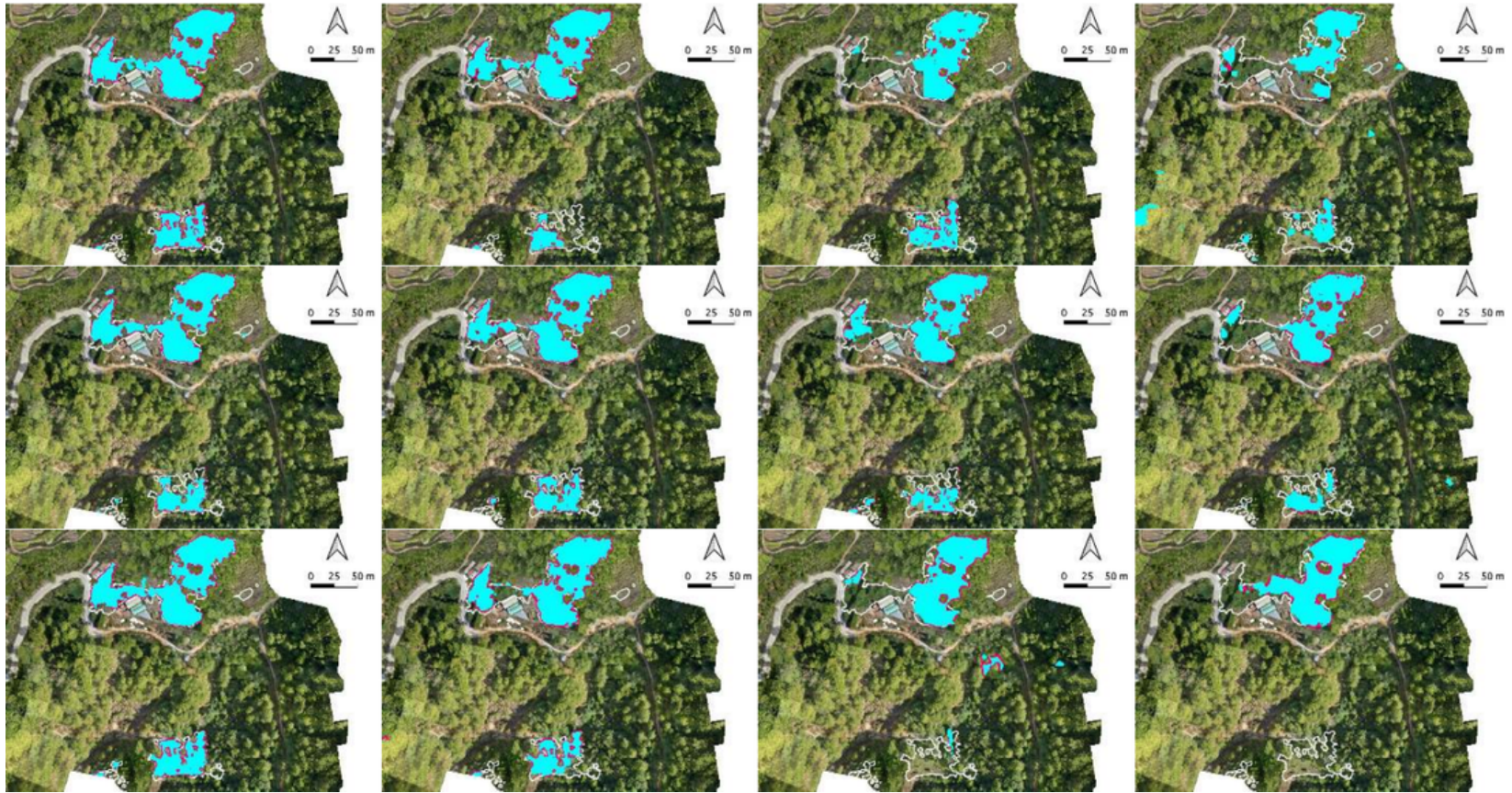


Figure L.7: Visualization of performance degradation on Chayote with decreasing GSD. Degradation methods: A, top row; B, center row; C, bottom row. GSDs per row in m/px, from left to right: 0.10, 0.15, 0.30, 0.50. Starting from 0.3 m/px, performance starts to degrade across all methods, whereas segmentation performance going from 0.10 m/px to 0.15 m/px is only affected less.

M Exemplary applications of the Cording Index

M.1 GSD prediction for vineyard leave density estimation

[61] studied the ability of multiple machine learning models such as support vector regression and k-nearest neighbor to estimate the leaf area index (LAI), which measures the total leaf area for a given ground area, indicating the density of leaves. The study was conducted over a small vineyard in Turpan city, Xinjiang, China, where (according to [61]) the most widespread grape vine variety is *Vitis vinifera*.

The authors found that for two GSDs, 0.007 and 0.045 m/px, the R^2 values of their best model were 0.825 and 0.637, respectively, when using RGB imagery to estimate LAI.

The leaves of the *Vitis vinifera* variety are heart-shaped, and approximately 5–15 cm wide [70, 71]. CI then produces the interval ($\frac{0.05}{3} \approx 0.016$, $\frac{0.15}{3} = 0.05$). Based on the two provided R^2 values, this is a sensible range for where performance deteriorates.

M.2 GSD prediction for cows and sheep

In [30] it was found that mean average precision (mAP) for detecting cows dropped sharply starting around 0.15–0.20 m/px. Although the species of cow was not specified, average body width of common cow breeds lies between 51.7–69 cm [72, 73, 74, 75]. Many cows in the study had black fur [30], so their bodies (rather than fur texture) were chosen as SVA. The SVA was measured as body width because it is the shortest axis for cows in overhead imagery.

CI then gives a GSD interval of ($\frac{0.517}{3} \approx 0.172$, $\frac{0.69}{3} = 0.23$), which matches the observed start of performance degradation well. Additionally, GSDs beyond 0.23 resulted in mAPs of 0.6 or lower, from the initial score of about 0.95, so the metric also provides a sensible cutoff point.

The mAP for sheep in [30] was initially more stable for three of the four employed degradation methods, remaining close to 1, decreasing at a GSD around 0.2 m/px and dropping sharply at 0.3 m/px. For the circular degradation method with input size 1280x1280 (“1280 Circular”), performance decreased slightly at a GSD of 0.1 m/px, and dropped sharply at 0.2 m/px.

Width of domestic sheep is not well documented, but [76] reports a body width of 44–66 cm. The interval derived via CI is ($\frac{0.44}{3} \approx 0.147$, $\frac{0.66}{3} = 0.22$). This estimate suits the observed degradation trends well. In particular, the lower bound lies before significant decreases across all four degradation methods, and the upper bound is tight enough to provide a suitable cutoff also for the 1280 Circular degradation method.

N Effect of target pixel density on survey characteristics

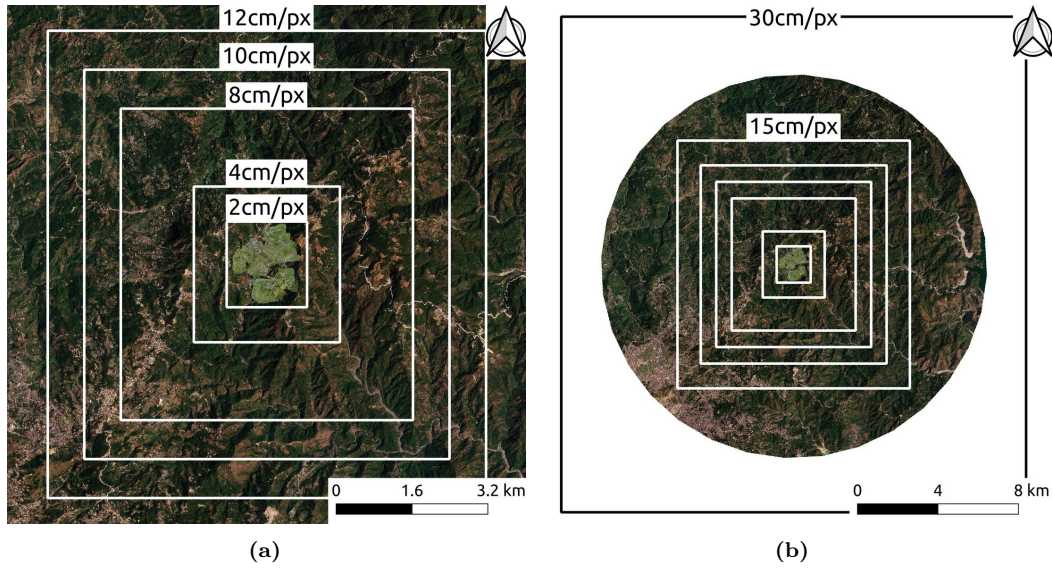


Figure N.8: Change in geographic extent relative to spatial resolution when fixing image dimension (in pixels) to native dataset resolution at 0.022 m/px. (a) Sto. Niño dataset overlaid onto Planet satellite imagery, with bounding boxes for 5 VHR GSDs; (b) additional extents for 0.15 and 0.3 m/px GSDs. The satellite basemap covers an area of approximately 286.27 km². Extents for remaining resolutions above 0.30m/px fall outside the figure.

Table N.5: Estimated flight statistics for a DJI Mavic 3M drone imaging each region shown in Fig. N.8, such that the number of pixels in each orthomosaic is the same as for the native dataset with a GSD of 0.022 m/px. Statistics for GSDs of 3, 5, 10, and 15 m/px not shown as the maximum flight altitude of 6km would be exceeded. The maximum legal flight height in most countries is 120 metres, thus a lower quality sensor would need to be fitted on the drone, rather than increasing altitude as shown here. Calculations are based on the specifications provided by DJI.

GSD (m/px)	Altitude (m)	Area to image (km ²)	8h workdays to complete imaging (optimistic estimates)
0.022	75.08	3.06	0.30
0.04	150.16	10.12	1.34
0.08	300.32	40.48	2.22
0.10	375.40	63.26	4.44
0.12	450.48	91.09	5.55
0.15	563.098	142.32	6.66
0.30	1126.20	569.30	8.33
0.50	1876.99	1581.38	16.66
0.70	2627.79	3099.50	27.76
1.00	3753.99	6325.51	38.87

O Example of EcoMapper applicability

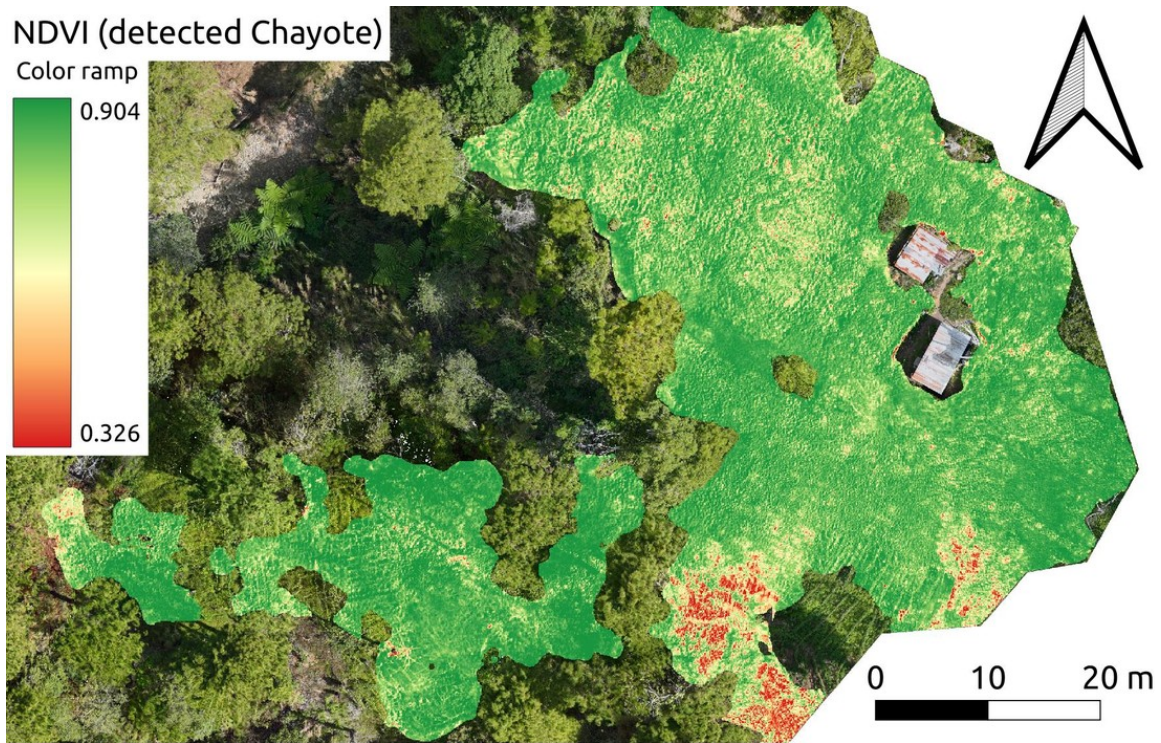


Figure O.9: Normalized difference vegetation index (NDVI) for a Chayote plantation in the test set, using the model's predictions as mask. The NDVI indicates plant health and lies between -1 and 1. By masking the NDVI map, it shows the health of Chayote plants relative to each other, which helps identify which areas need irrigation or treatment.